Passive Tracer Modelling at Super-Resolution with WRF-ARW to Assess Mass-Balance Schemes

Sepehr Fathi[1,3], Mark Gordon[2], and Yongsheng Chen[2]

[1]Physics and Astronomy Department, York University, Toronto, Canada
[2]Earth and Space Science and Engineering Department, York University, Toronto, Canada
[3]Air Quality Research Division, Environment and Climate Change Canada, Toronto, Canada

Correspondence: Sepehr Fathi (sfathi@yorku.ca, sepehr.fathi@ec.gc.ca) and Mark Gordon (mgordon@yorku.ca)

Abstract. Accurate "super-resolution" ($\Delta x < 250$ m) atmospheric modelling is useful for several different sectors (e.g., renewable energy, natural disaster prediction), and essential for numerous applications such as downscaling of weather and climate information to finer resolutions. It can also be used to interpret environmental observations during top-down retrieval campaigns by providing complementary data that closely correspond to real-world atmospheric pollution transport and dispersion conditions. In top-down retrievals (e.g., aircraft-based), errors in estimates can arise from assumptions about atmospheric dispersion conditions, uncertainties in measurements, and data processing. As discussed in this work and in Fathi (2022), super-resolution numerical model simulations can be utilized to investigate these sources of uncertainty and optimize the retrievals. In order to conduct a thorough model-based study of the atmospheric dynamical processes that can affect top-down retrievals, model simulations at super-resolutions on the scale of measurement frequency are required: sufficient to resolve the dynamical and turbulent processes at the scale at which measurements are conducted. Here, in the context of our modelling case studies with WRF, we demonstrate a series of best practices for improved (realistic) modelling of atmospheric pollutant dispersion at super-resolutions. These include careful considerations for grid quality over complex terrain, sub-grid TKE parameterization at the scale of large eddies, and ensuring local and global tracer mass-conservation.

For this work, super-resolution ($\Delta x \leq 50$ m, $\Delta t \leq 1$ s) model simulations with Large-Eddy-Simulation sub-grid scale parameterization were developed and implemented using WRF-ARW. The objective was to resolve small dynamical processes inclusive of spatio-temporal scales of high-speed (e.g., 100 m/s) airborne measurements. This was achieved by down-scaling of reanalysis data from 31.25 km to 50 m through multi-domain model nesting in the horizontal and grid-refining in the vertical. Further, WRF dynamical-solver source code was modified to simulate passive-tracer emissions within the finest resolution domain. Different meteorological case studies and several tracer emission sources were considered. Model-generated fields were evaluated against observational data and also in terms of tracer mass-conservation. Results indicated model performance within 5% of observational data in terms of sea level pressure, temperature and humidity, and agreement within one standard deviation between modelled and observed wind fields. Model performance in terms of tracer mass conservation was within 2% to 5% of model input emissions.

1 Introduction

Generating model simulations of atmospheric processes at high spatial and temporal resolutions (super-resolution) have numerous applications including hybrid physical-model and machine-learning applications (Onishi et al., 2019), the dynamic downscaling of coarse resolution climate and weather information (Watson et al., 2020), and urban-climate feedback studies (Wu et al., 2021). Super-resolution modelling products ($\Delta x < 100$ m, $\Delta t < 1$ s) can also provide desirable information at the scale of measurements during top-down campaigns, which can be analyzed in conjunction with measurement data to: interpret observations, quantify uncertainty in the measurements, test the validity of assumptions in the employed top-down methodologies, and help fill the information gap in measurements. In the context of mobile platform (e.g., aircraft) top-down source emission rate estimations, numerical model simulations can be employed in various approaches. These include off-line applications, where a meteorological model (e.g., Weather Research and Forecasting - WRF) is used to replicate conditions during airborne and/or ground-based observations. The model generated meteorological fields are often used to drive a separate Lagrangian tracer dispersion model (e.g., HYSPLIT) either forward in time to simulate tracer concentrations at observation times and locations, or for inverse method analysis (Cui et al., 2015; Lauvaux et al., 2016; Kia et al., 2022). Previous airborne studies have also used model generated wind fields and aircraft measured concentrations for flux calculations and mass-balance analysis (Karion et al., 2015). The emission and transport of passive tracers can be simulated in-line with meteorological fields within the same modelling platform such as the Eulerian WRF model, for source emission characterizations at the scale of observations (Ahmadov et al., 2015; Barkley et al., 2017; Nahian et al., 2020). For these applications, model generated fields are analyzed as complementary information for characterizing emissions based on airborne observational data. For instance, Ražnjević et al. (2022) have employed large-eddy-simulation (LES) modelling driven by reanalysis data for interpreting field observations of CH_4. Further, model simulations of tracer transport and dispersion have been previously used for assessing the uncertainties/errors in top-down retrievals and optimizing the observational approach (Conley et al., 2017; Fathi, 2017; Angevine et al., 2020; Fathi et al., 2021; Fathi, 2022). Numerical model simulations can also be used for simulating ground-based and/or airborne observations, where model generated fields are used as a proxy for measurement data (virtual sampling). For a robust model-based study of observational methods, model resolutions must be chosen to resolve the time and length scales of the measurements. For example, Gasch et al. (2020) simulated aircraft-based Doppler Lidar measurements of wind fields through LES modelling at 10 m resolution to investigate airborne lidar measurements for a lidar range length of 72 m.

Fathi et al. (2021), used a regional chemical transport model with physical and chemical process representations (GEM-MACH), and were successful in evaluating the application of the mass-balance technique in top-down retrievals using model simulated fields as a proxy for the real world environmental fields. However, the relatively coarse resolution (2.5 km, 2 min) of the employed model was insufficient for the investigation of aircraft-based retrievals through virtual airborne samplings within the model simulated 4D fields. In airborne campaigns, environmental observations (e.g. wind, temperature, tracer concentrations) are made while flying downwind or around emission sources. These data are then processed through various retrieval algorithms to estimate source emission rates (Peischl et al., 2010; Ryoo et al., 2019; Gordon et al., 2015). An underlying assumption common among retrieval algorithms is the steady-state conditions during the sampling time of several hours (Alfieri

et al., 2010). Data collection during aircraft-based in-situ measurements are made through 3D space and over time, thus: (a) any point in space along the flight path is visited only once, and (b) spatially adjacent data points are collected at different (consecutive) times. By assuming stationarity (e.g., wind, emissions), the observational data are assumed to be representative of the average conditions during the sampling time. However, time-varying conditions (whether due to turbulence or weather trends) can reduce the representativeness of the sparsely collected environmental data. To study these effects through model simulations, the model resolutions should be chosen to resolve dynamical processes (turbulence) at the spatio-temporal scales at which aircraft in-situ measurements are made. For instance, to simulate (and evaluate) in-situ measurements at a flying/sampling speed of 100 m/s (e.g., onboard instrument sampling frequency $\geq$ 1Hz: Conley et al., 2017; Gordon et al., 2015), the model should be able to simulate (and output) atmospheric fields at length and time scales of $\Delta x \leq 100$ m and $\Delta t \leq 1$ s. Recent real-case LES-modelling studies have commonly referred to such resolutions ($\Delta x \leq 250$ m) as "**super-resolution**" (e.g., Wu et al., 2021; Onishi et al., 2019; Watson et al., 2020), herein we use the same terminology to describe our WRF model simulations.

The modelling requirements described above, motivated the development of super-resolution micro and LES scale atmospheric tracer transport model simulations, fine enough to resolve smaller-scale flow details and the effects of turbulence and changing stability in atmospheric mixing of tracer concentrations downwind of point and area sources of emission, enabling:

1. thorough dynamical evaluation of the application of the divergence theorem and the mass-balance technique in inferring source emission rates,

2. investigating the effects of flight pattern in aircraft-based top-down retrievals, utilizing model 4D output database,

3. exploring improved sampling approach through optimized flight design and multi-platform (in-situ, remote) sampling,

4. exploring improved data analysis, post-processing, and interpolation/extrapolation methods needed for flux calculations based on airborne observations.

In this study, we present a proof of concept for performing super-resolution model simulations of atmospheric tracer transport and dispersion using WRF with the ARW (Advanced Research WRF) dynamical solver core. The concepts that are explored here include (a) the realistic modelling of the atmospheric boundary layer at large-eddy-simulation scale over complex terrain, (b) the mass-conserved modelling of atmospheric dispersion and transport of passive tracers under the conditions described in (a), and (c) generating modelling products at spatio-temporal scale of airborne observations (aircraft-based in-situ and remote measurements), useful for evaluating the observational methods and providing recommendations for future studies. We evaluate the performance of our model simulations against historical observational data from ground-based monitoring stations and aircraft-based observations from the 2013 airborne campaign the Joint Canada-Alberta Implementation Plan on Oil Sands Monitoring (JOSM, 2013). We further assess the performance of our simulations in terms of global (over the entire modelling domain) and local (sub-domain) mass-conservation, by conducting 4D mass-balance analysis.

We explore three different cases (dates and times) during August and September of 2013 over Canadian oil sands (Athabasca, Alberta). We use reanalysis data as initial and boundary conditions for our case studies. To achieve the desired micro and LES

scale resolutions, we perform multi-domain nested simulations with LES parameterization for the finest domains. Further, we modify the WRF source code (dynamical solver) to simulate the release of passive tracers from points and area sources within the finest model domain. The novel modelling approach with WRF presented in this work is comprised of: (1) dynamical downscaling of reanalysis data from synoptic to LES resolution, (2) super-resolution model simulations through horizontal nesting and vertical grid refining, (3) LES sub-grid parameterization, and (4) passive tracer transport and dispersion simulations. To our knowledge, the combination of these capabilities in WRF modelling has not been explored extensively in the past where reanalysis-driven super-resolution dispersion modelling under local mass-conservation condition is conducted. In this work we discuss a series of modelling best practices for such simulations in the context of our case studies, for improved modelling of atmospheric pollutant dispersion. The modelling approach in this work is geared towards the assessment of mass-balance methodologies, but throughout we discuss the general usefulness of super-resolution modelling for generating highly resolved (spatial and temporal) pollutant dispersion forecasts and their potential application in measurement planning and interpreting the observations. The model output data from the super-resolution simulations in this work are also used for evaluating the accuracy of aircraft-based emission rate retrieval methodologies in Fathi (2022).

2   Methods

2.1   Case Studies

For this work we chose our case studies from the times and locations of three emission estimation flights during the JOSM 2013 campaign over the Athabasca oil sand region (Alberta, Canada). This choice was made to enable qualitative comparisons to observations. We considered the geographical location of an oil sands facility, Canadian Natural Resources Ltd. (CNRL). We configured our WRF model domain centred over the CNRL facility. For our WRF simulations, we considered model simulation times overlapping those of three JOSM 2013 box flights over CNRL (see Table 1). Box flight refers to closed shape (e.g. rectangular, cylindrical) flight paths around the target emission source, where aircraft-based measurements are used to estimate source emission rates using the mass-balance technique (Gordon et al., 2015). Note that case 2 on 26 August 2013 was a "rejected" case in the actual campaign analysis due to unsuitable atmospheric conditions for aircraft-based retrievals (Fathi et al., 2021), but it is analyzed here as an assessment of the super-resolution model.

Table 1. Three case studies during late August and early September of 2013 over oil sands facility CNRL. Times and locations for the case studies where chosen from three JOSM 2013 box flights.

	Case 1	Case 2	Case 3
Date	20 Aug	26 Aug	2 Sep
Start Time (Local Time)	10:30	13:43	11:43
Start Time (UT)	16:30	19:43	17:43
Duration (hh:mm)	02:10	01:52	01:45
Model Simulation Time	15UT - 19UT	18UT - 21UT	15UT - 19UT

For each of these three cases, eleven tracer emission scenarios/sources are considered. Table 2 provides the spatial details for the different emission sources, including seven elevated point sources (representing stack emissions), two small area sources (representing surface mines), a large area source (representing the tailing pond west of CNRL) and a long multi-section line source (over the approximate extent of the Horizon Highway south of CNRL). Table 2 lists geographical coordinates and tracer release heights (stack top height) for all of the sources. Horizontal dimensions are also provided (in brackets) for the line and area sources. The horizontal dimensions for each of the point sources are equal to those of one grid cell in the finest model domain. Coordinates and heights for CNRL1-4 correspond to actual (real world) stacks in the CNRL facility. The hypothetical source CNRL0 is co-located with CNRL1 and 4, with stack-top/release height at over 4 times higher than the tallest facility stack (CNRL1), simulating the initial (assumed instantaneous) plume rise due to buoyancy. Figure 1 shows a map of the region with the location and spatial extent of case study emission sources marked/labelled in red. The large rectangular area (surface) source represents the tailings pond on the west of the CNRL complex. The multi-segment line (surface) source represents the Horizon Highway south of CNRL. Two small area sources labelled as Mine 1 and Mine 2 represent emissions from surface mine excavation sites within the CNRL complex. Figure 1 also shows the locations for two hypothetical point (stack) sources CNRLs (south) and CNRLw (west). During two of our case studies on 20 August 2013 (case 1) and 2 September 2013 (case 3), the mean wind was from west and south-west, placing these two hypothetical stacks upwind of the CNRL facility.

Table 2. Eleven tracer emission scenarios including seven point sources representing release from stack tops at various heights, three area sources including a large area tailing pond towards the western side of the facility and two smaller (in area) surface mines, and a line source approximately spanning the extent of the Horizon Highway south of the facility. Note that height/locations for sources with superscript ‡ are hypothetical.

Source ID	Type	Lat.	Lon.	Spatial Extent	Height agl (m)	Description
CNRL0[‡]	Point	57.339	-111.738		483	Stack
CNRL1	Point	57.339	-111.738		114	Stack
CNRL2	Point	57.337	-111.740		54	Stack
CNRL3	Point	57.336	-111.732		30	Stack
CNRL4	Point	57.339	-111.738		54	Stack
CNRLw[‡]	Point	57.327	-112.014		102	Stack (upwind west)
CNRLs[‡]	Point	57.250	-111.867		102	Stack (upwind south)
HWY	Line	57.258	-111.765	$\sim$20 km	6	Horizon Highway
POND	Area	57.348	-111.918	$\sim$50 km^2	6	Tailing Pond
MINE1	Area	57.337	-111.834	550 m $\times$ 550 m	6	Surface Mine 1
MINE1	Area	57.325	-111.820	350 m $\times$ 550 m	6	Surface Mine 2
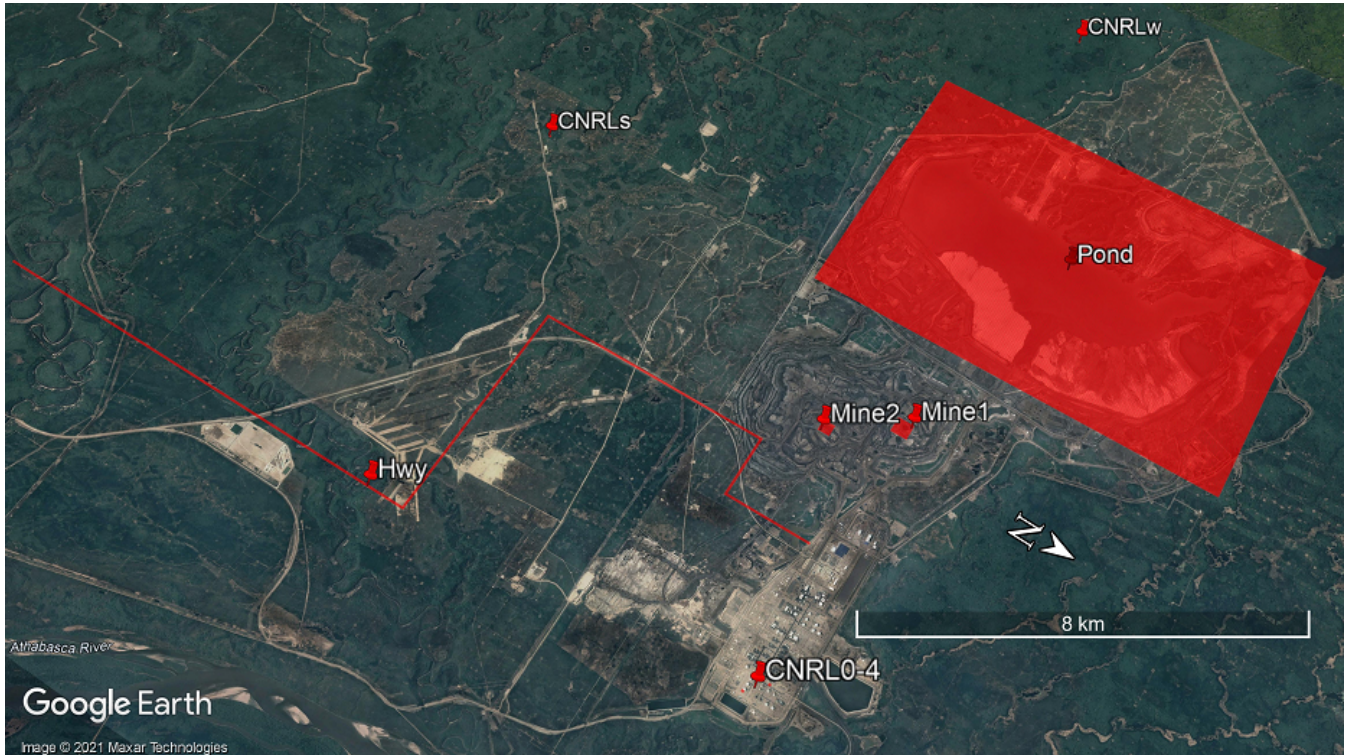
Figure 1. © Google map (2021) of the study region: The oil sands facility CNRL with case study emission sources marked on the map including seven point sources, two area sources, a large area surface source (tailing pond) and a multi-segment line source (road/highway). Direction of north (N) is shown with a compass arrow.

2.2 Model and Technical Setup

For this work, the Weather Research and Forecasting (WRF - Skamarock et al., 2008) model with the ARW dynamical core was utilized. WRF-ARW provides a multi-scale simulation framework suitable for efficient parallel computing with a vast range of physical parameterizations adaptable for different scales and dynamical processes. The Advanced Research WRF (ARW) solver features a suite of fully-compressible Euler-nonhydrostatic equations for solving prognostic variables including velocity components in Cartesian coordinates (u, v, w), and scalars such as water-vapour mixing ratio and tracer concentration. The 3rd order Runge-Kutta scheme (RK3) is used for time integration in ARW (Wicker and Skamarock, 2002). The spatial discretization in WRF-ARW uses a Arakawa C-grid staggering with thermodynamics/scalar variables (e.g., moisture, tracer) defined on grid cell centres (mass points), and velocity components defined normal to respective faces of model grid cells (one-half grid length from mass points). 2nd to 6th order spatial discretization and RK3 time-integration scheme are available in ARW to solve for advection of momentum, scalars, and geopotential in flux form (the governing equations). The RK3 transport/advection (combined with flux divergence) in WRF-ARW is conservative, however it does not guarantee positive definiteness on its own. Negative mass creation is offset by positive mass such that tracer/scalar mass is conserved over the

modelling domain (Skamarock et al., 2008). Negative mass can be set to zero, but this will result in erroneous increase of tracer mass within the modelling domain. By choosing a positive-definite scalar advection option in WRF-ARW, as we did in our simulations, a flux re-normalization is applied to the transport step to remove the nonphysical effects such as creation of the negative mass (Skamarock and Weisman, 2009). To Summarize, if the outgoing fluxes (removing mass from the control volume) in the final step of RK3 predict a negative updated scalar/tracer mixing ratio, the outgoing fluxes are re-normalized to be equivalent to mass within the volume. For more details see Section 3.2.3 in Skamarock et al. (2008). Various formulations are available in ARW solver for explicit spatial diffusion (turbulent mixing) including a sixth order spatial filter proposed by Xue (2000). The implementation of this scheme in ARW is described in Knievel et al. (2007). The sixth order turbulent diffusion scheme is also prone to creating negative mass due to negative up-gradient diffusion. Monotonicity can be enforced in the model (user specified option) by setting negative diffusive fluxes to zero, however it does not conserve scalar mass (Skamarock et al., 2008). Hence, in our simulations we used the sixth order diffusion scheme without the monotonic option.

Mesh refinement and increased resolution can be achieved in WRF through series or concurrent grid nesting in the horizontal dimensions. With concurrent grid nesting, multiple computational domains with increasing resolution can be integrated simultaneously. The process where the coarse "parent" domain's output is interpolated to provide initial and lateral boundary conditions for the fine "child" domain, a process referred to as one-way nesting. Two-way nesting is achieved when information from the "child" domain is aggregated to write the overlapping regions of the "parent" domain. At high resolutions (< 3 km), mesh refining in WRF via grid nesting only in the horizontal dimensions limits the control over the grid aspect ratio which can lead to poor grid quality and numerical errors. It has been shown that grid quality affects the accuracy of numerical solutions (Lee and Tsuei, 1992; You et al., 2006). A procedure permitting vertical nesting for one-way concurrent simulation is developed and described in Daniels et al. (2016), which allows high resolutions in the order of meters while grid quality is maintained. This procedure permits one-way concurrent grid nesting in both the horizontal and vertical and this is herein utilized for WRF simulations with 5 domains (d01 - d05) with increasing resolutions from ~ 31 km to 50 m in the horizontal dimensions and up to near surface vertical resolution of ~ 10 m in the finest domain d05.

With regards to nesting in the horizontal, Skamarock et al. (2008) recommended the use of odd nesting ratios such as 1:3 and 1:5 (as opposed to even ratios like 1:2), due to the staggered structure of the Arakawa C-grid used in WRF-ARW modelling framework. Mohan and Sati (2016) investigated the impact of different nesting ratios in WRF and found no statistically significant difference in simulated results with ratios 1:3, 1:5, and 1:7, suggesting that larger ratios can be used to reduce the computational cost in nested simulations. However, larger ratios (e.g., 1:9) can result in increased interpolation errors and are not recommended. In this work, as a compromise between numerical accuracy and computational cost, we used a 1:5 nesting ratio. Figure 2a shows the 5 domains of the model and their relative size. Model domains are centred on the region of Athabasca oil sands with the two finest domains (d04 and d05) centred on the CNRL Horizon facility on the north west quarter of the complex, west of the Athabasca river. Figure 2b shows a map of the region with the CNRL facility marked on the map (red star). Boundaries of the two finest domains, d04 and d05, are also overlaid on the map in Figure 2b. The relative location of the other oil sands facilities can be seen in the figure. CNRL is at the north west corner of the complex with no facilities to its north and west. The oil sands region is located on the Athabasca river valley with 400-500 m vertical relief within a few tens

Table 3. Case study model setup for model simulations with 5 domains with increasing resolution. The first 3 domains have the same coarse vertical grid. Domains d04 and d05 have increasing resolution via vertical grid refinement. The finest domain (d05) has $\Delta z \simeq 12$ m for the first 40 levels near the surface. Δx and Δt indicate the horizontal grid size and the model simulation time-step for each domain, respectively. X and Y indicate domain dimensions. nx, ny and nz are the number of computational grid points in each direction. With model top layer at 15.623 km (15.350 km agl) and pressure level 10 kPa for all domains.

Domain	Vertical grid description	Δx(m)	Δt(s)	X(m)	Y(m)	nx	ny	nz
d01	Coarse grid	31250	100	6281250	6281250	201	201	30
d02	Same as d01	6250	20	3131250	3131250	501	501	30
d03	Same as d01, d02	1250	4	751250	751250	601	601	30
d04	d03 grid refined ($\sim$1:3) below 2500 m agl	250	0.8	175250	175250	701	701	48
d05	d04 grid refined ($\sim$1:7) below 540 m agl	50	0.16	50050	50050	1001	1001	83

of kilometres of the facilities (mainly in the west-east direction). This may give rise to complex flow conditions and frequent vertical wind shear in the valley (Gordon et al., 2018). In section 3.2 we discuss the performance of our super-resolution model simulations against observed meteorology for the same locations and time periods.

The North American Regional Reanalysis (NARR) GRIB data (at 3 hour intervals) from NOAA (National Oceanic and Atmospheric Administration) archives were used, for August and September of 2013 (period of JOSM 2013 campaign) over the Athabasca oil sands region (Alberta, Canada). Realistic WRF-ARW simulations were carried out with concurrent one-way grid nesting in the horizontal dimensions with 5 domains (d01-d05) at a ratio of 1:5 and with mesh grid refinement in the vertical for the two smallest and finest domains (d04 and d05) by consecutively increasing the number of vertical levels near the surface. The finest domain (d05) has a horizontal grid size of $\Delta x = 50$ m over the entire domain, $\Delta t = 0.16$ s model simulation time-step and $\Delta z = 11.62$ m for the first 40 full grid levels near the surface. Note that the vertical resolution of about 12 m for the bottom 500 m agl (above ground level) is sufficient for investigating and evaluating different methods for extrapolating sampled data below the lowest flight level (typically $\sim$ 150 m) where no aircraft-measurements are usually made, which is required for flux estimations in top-down emission rate retrieval methods (Gordon et al., 2015). Further, note that Δx and Δt configurations are set as such to ensure Courant-Friedrichs-Lewy (CFL) stability criterion, $\Delta t < \Delta x/|u_{max}|$ where $|u_{max}|$ is the maximum wind speed in the model (Jacobson, 2005). Table 3 provides the details of model grid configurations for the five domains. In order to simulate small-scale atmospheric dynamical processes, the finest two model domains (d04 and d05) were configured with the following dispersion scheme, and Large Eddy Simulation (LES) sub-grid parameterization options available in the WRF model (Skamarock et al., 2008),

1. Diffusion option was set to "Full Diffusion" mode (*diff_opt*= 2) to accurately compute horizontal gradients using full metric terms.

2. The horizontal diffusion option was configured with the 6th Order diffusion scheme (*diff_6th_opt*= 1).
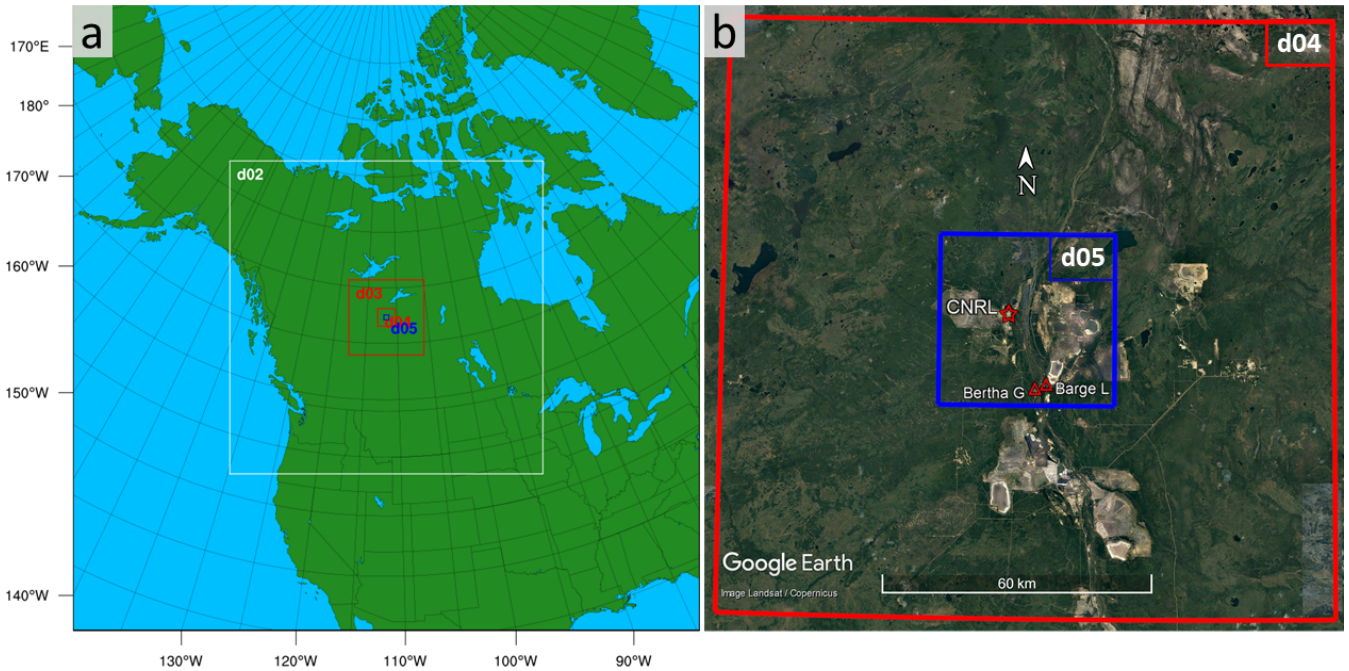
Figure 2. (**a**) WRF model grid (horizontal) configuration with five nests d01 - d05 with increasing resolution (decreasing size) at a ratio of 1 to 5. The finest domain, d05, is centred over the oil sands region. (**b**) © Google map (2021) of the oil sands region with overlay of model domains d04 and d05. The CNRL facility is marked with a red star. Locations for two WBEA monitoring stations are also shown with red triangles, Bertha Ganter – Fort McKay and Barge Landing monitoring stations.

   3. "K Option" was set to *km_opt*= 2 to solve a prognostic equation for turbulent kinetic energy (TKE) where the diffusion
200   coefficient K is calculated based on TKE (see Appendix A).

WRF 3.7+ includes a basic framework for initiating and creating continuous (and variable) emission tracer plumes. To simulate the emission of passive-tracers, the WRF dynamical-solver source code was modified following an approach similar to Blaylock's (as described in Blaylock, 2017) used in Blaylock et al. (2017). Tracer amounts were initiated at several different horizontal locations within the finest domain (d05) after 30 minutes model simulation. A meteorological spin-up time of 1 hour

205 was considered through testing with the modelling setup for different initial and boundary conditions according to the following criteria: for the cases we considered, within the first hour of simulation time (a) the model boundary conditions propagated over the entire span of domain d05, (b) model winds (in west-east and south-north directions) assumed continuous profiles both horizontally and between model vertical layers, (c) water vapour on model mass-layers (horizontal and vertical mass grid points) assumed continuous profiles within this time period. Tracer release for our considered emission scenarios (see Table 2)

210 started after a 30 min spin-up time (half the meteorological spin-up time) and continued for the rest of the simulation period. These included surface emissions on several model grid points at the lowest level (i.e., level 1 at ∼ 6 m agl) at various locations, and stack emissions at levels 3, 5, 9, 10 and 40 according to the stack top heights and horizontal locations described in Table

2. Note that in WRF-ARW vertical levels (Fig. S1) are configured using a terrain-following hydrostatic-pressure coordinate system (Skamarock et al., 2008) and therefore stack-top heights for our simulations are assigned to pressure levels with heights (in meters) closest to source heights. Depending on pressure changes, the height of pressure levels can vary over time. This variation was determined to be smaller than the corresponding vertical level thickness for our simulations and therefore its impact on tracer release simulation is considered negligible in this work. All of the tracer emissions were implemented within the boundaries of the CNRL facility and the surrounding region, on the eastern half of the modelling domain. All the emission scenarios involved the emission of passive and non-buoyant tracers with no interactions with meteorology and no defined surface deposition rates. Note that the topography input information (land use indices) used in our WRF simulations were not modified to represent oil sands operations (e.g., tailing pond, excavation sites) and only represent natural features (e.g., river basin, hills). The release, dispersion and transport of tracers from our emission scenarios under different meteorological conditions are discussed in the Section 3.3.

2.3 Divergence Theorem and the Mass-balance Technique

For this work, the mass-balance technique is utilized for calculating the net integrated flux out of virtual control volumes (emission box) enclosing the emission sources of interest. The calculation steps in this section follow those in Fathi et al. (2021), with slight modifications for use with WRF model output data. For a detailed discussion on the application of the mass-balance and divergence theorem in estimating source emission rates see Fathi et al. (2021).

In applying the mass-balance technique to estimate the rate of emissions from sources within a flux box (control volume), the mass flux exiting the box through box top and lateral walls are equated to the emission rate of the tracer within the box. The processes contributing to the change of mass, for a passive tracer, within the control volume can be described with the following expression,

$$S_C = E_C - F_{C,H} - F_{C,V} - F_{C,HT} - F_{C,VT} \tag{1}$$

where the storage term S_C represents the change in mass of tracer C within the control volume, E_C represents the tracer emission rate, $F_{C,H}$ and $F_{C,V}$ represent the net horizontal and vertical advective fluxes exiting through lateral and top walls of the flux box, respectively. $F_{C,HT}$ and $F_{C,VT}$ represent horizontal and vertical turbulent fluxes across the box walls, respectively.

The total mass of the tracer within the control volume can be calculated by integrating the mass over the entire volume of the box at each model output timestamp ($\Delta t = 1$ sec),

$$B_{C,Tot}(t) = \iiint \chi_C(t,x,y,z)dxdydz \tag{2}$$

where $\chi_C(t,x,y,z)$ is the tracer concentration at each model grid point. Further the storage term can be calculated by taking the time derivative of $B_{C,Tot}(t)$,

$$S_C(t) = \frac{\partial}{\partial t}B_{C,Tot}(t) \tag{3}$$

Horizontal advective flux through the lateral walls of the box can be calculated by extracting tracer concentration and normal wind (positive outwards) along the lateral walls of the box from model output,

$$F_{C,H}(t) = \iint \chi_C(t,s,z) U_\perp(t,s,z) ds(x,y) dz \tag{4}$$

where $ds(x,y)$ is the path $s(x,y)$ increment along the walls. $U_\perp$ is the normal wind to the box walls (positive outwards).

Similarly, the vertical flux through the box top can be calculated as,

$$F_{C,V}(t) = \iint \chi_{C,top}(t,x,y) W_{top}(t,x,y) dx dy \tag{5}$$

where $\chi_{C,top}(t,x,y)$ and $W_{top}(t,x,y)$ are tracer concentration and vertical wind speed at box top, respectively. See Appendix B for turbulent flux terms. As we show later, the vertical advective ($F_{C,V}$) and the turbulent fluxes ($F_{C,HT}$, $F_{C,VT}$) have negligible relative contributions to the mass-balance equation, with the horizontal advective flux $F_{C,H}$ being the dominant term removing mass from the box. We collect all the flux terms (advective and turbulent) contributing to the removal of tracer mass from the box into a single flux out term as $F_{C,out} = F_{C,H} + F_{C,V} + F_{C,HT} + F_{C,VT}$. By rearranging Eq. 1, the tracer emission rate can be estimated based on the other terms as,

$$E_C = S_C + F_{C,out} \tag{6}$$

By extracting the required fields from the model output 4D database, Equation 6 can be utilized to determine the source emission rate based on the mass-balance equation which can then be compared to the known input emission rate. Following the above described calculation process, source emission rates can be estimated at each model output time-step and compared to the model input emissions to evaluate model performance in terms of local mass-conservation and mass-flux consistency. See Table S1 for discrete integral expressions of different terms in the mass-balance equation (Eq. 6). Note that for flux calculations in this work, model wind fields were linearly interpolated onto the mass grid-points (where concentration fields are defined).

3 Results and Discussions

Model simulations were carried out for the period between 15UT to 19UT for cases 1 and 3 on 20 August and 2 September 2013, respectively. The simulation period for case 2 on 26 August 2013 was between 18UT to 21UT (see Table 1). NARR reanalysis data at 31.25 km resolution was used as initial and boundary conditions for the coarsest domain d01 with the same resolution. Through model nesting at an increasing resolution (and decreasing size) ratio of 1:5, the input reanalysis data were down-scaled to consecutively higher resolutions all the way to 50 m in the finest domain d05. Each parent domain provided initial and boundary conditions for their nested child domain: d01 ⇒ d02 ⇒ d03 ⇒ d04 ⇒ d05. Note that feedback (two-way nesting) between parent and nested domain was turned off to allow for vertical grid refining for domains d04 and d05. Output frequency was set to 3 hours for domains d01 – d03, 100 seconds for d04, and 1 second for d05.

Table 4. Evaluation of domain d05 simulations against d04 output fields at every 100 seconds at the geographical location of the CNRL oil sands facility (Lon=-111.738 and Lat=57.339). Note that positive/negative sings indicate over/under-estimates by d05 relative to d04.

		SLP (hPa)	2m RH (%)	2m T (°C)	10m U (m/s)	10m V (m/s)
	d04 mean	1006.42	51.18	19.32	5.05	3.20
Case 1	rms error	0.11	1.89	0.25	3.16	1.37
	mean error	-0.04	-1.20	-0.17	3.11	1.14
	d04 mean	1013.44	52.59	20.30	-0.766	0.799
Case 2	rms error	0.56	7.59	1.84	0.59	2.20
	mean error	0.55	6.86	-1.81	-0.55	-2.16
	d04 mean	1006.14	62.40	21.95	3.57	3.90
Case 3	rms error	0.09	2.44	0.38	2.77	1.01
	mean error	0.06	-2.24	0.36	2.73	0.75

3.1 Model Sensitivity

Sensitivity analysis showed consistent performance by the 5 nested domains. For instance, output from the three finest domains (d03, d04, d05) for case 1 agreed to a great extent for sea level pressure with < 1 hPa difference, relative humidity (at 2 m agl) with 2% difference, and temperature (at 2 m agl) within 2-3 °C. Wind directions were also consistent with 2 to 7 degrees difference for a mean wind direction from about 240 degrees (west-south-west). Wind speeds were biased high relative to domain d03 with a mean wind speed of about 6 m/s, by 0.7 m/s to 1.5 m/s for domain d04 and by 3 m/s to 4 m/s for domain d05 (see Figure S2 for a comparison of wind vertical profiles from these three domains at 18UTC).

We also evaluated the performance of d04 and d05 simulations to d03 at the geographical location of CNRL. The evaluations were made in terms of east (U) and north (V) wind components, 2-m temperature, 2-m relative humidity and sea level pressure (see Figure S3 for case 1). Root mean square (rms) error scores were small (e.g., 0.5 m/s for U, 0.68 m/s for V, 0.45 °C for temperature) for d04 simulations at 250 m horizontal resolution and with LES parameterization. rms errors for d05 simulations were also similarly low for sea level pressure, temperature and humidity, with wind speed biased high by 1.57 m/s and 3.47 m/s for V and U respectively (at 10 m agl). As the model output data from domain d03 were only for every 3 hours, to evaluate the performance of domain d05 simulations at CNRL at a higher temporal resolutions we performed evaluations against domain d04 with model output every 100 seconds. Evaluation results for all three cases are summarized in Table 4. Root mean square (rms) error ranges from 0.09 hPa to 0.56 hPa for sea level pressure (SLP), 1.89 % to 7.59 % for 2-m relative humidity (RH), 0.25 °C to 1.84 °C for 2-m temperature, 0.59 m/s to 3.16 m/s for west-east wind component U, and 0.75 m/s to 2.20 m/s for south-north wind component V. For case 1 on 20 August 2013, 2-m temperatures ranged from 17 °C to 20 °C and 10-m wind speed from 6.6 m/s to 11.4 m/s at the geographical location of main CNRL stack sources. For case 2 on 26 August 2013, the 2-m temperature range was similar to case 1 but the 10-m wind speeds were much lower ranging from 0.8 m/s to 3.5 m/s with mean 2.8 m/s. For case 3 on 2 September 2013, 10-m wind speed ranged from 5.3 m/s to 9.4 m/s with 2-m temperatures
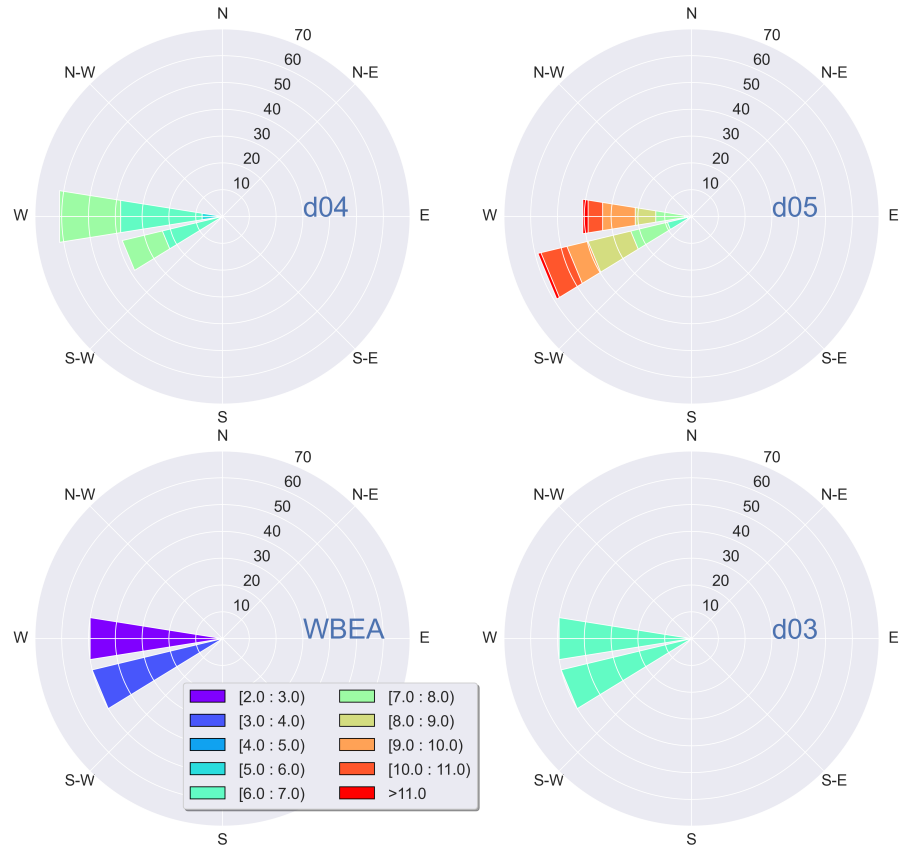
Figure 3. Wind-rose diagrams comparing observational data from WBEA monitoring station Bertha Ganter–Fort McKay to model output (case 1) winds at the location of the WBEA station from domains d03, d04 and d05 for 20 August 2013. Wind distributions, indicated on each circle, are in units of percentage. Wind directions are consistent within 20 degrees, blowing from W-S-W (towards E-N-E).

slightly higher than the other cases ranging from 21 °C to 23 °C. The temperature and wind speed ranges mentioned for the three cases are for periods between 18:00UT to 20:00UT (local noon to 2pm).

3.2 Meteorological Evaluation

295 Output from the finest three domains were compared to the concurrent historical observational data from the Wood Buffalo Environmental Association (WBEA) continuous monitoring stations Bertha Ganter – Fort McKay and Barge Landing for the periods of interest in August and September 2013 (https://wbea.org/historical-monitoring-data/). See Figure 2b for locations of the two WBEA stations on the map of the region (red triangles). We compared model 2-m relative humidity (RH), 2-m temperature and 10-m wind to the corresponding WBEA observational data. Model values at 2 m for domains d03-d05 and at

Table 5. Meteorological evaluation of domain d05 simulations against WBEA observational data at the geographical location of Bertha Ganter–Fort McKay (AMS01) station. Model performance is shown in terms of root mean square (rms) error and mean bias. Positive/negative values indicate over/under-estimates by d05 relative to WBEA-AMS01 observations.

		2-m RH(%)	2-m Temperature (°C)	10-m Wind Speed (m/s)	10-m Wind Direction (deg.)
Case 1	WBEA mean	44.52	22.97	2.85	244.96
	rms error	2.76	5.10	5.63	19.11
	mean bias	1.40	-5.08	5.60	11.26
Case 2	WBEA mean	83.90	19.61	2.08	93.5
	rms error	24.55	2.59	0.99	20.00
	mean bias	-24.54	-2.58	0.99	18.73
Case 3	WBEA mean	56.14	24.07	4.07	239.83
	rms error	5.81	2.29	3.37	169.70
	mean bias	-1.56	-1.97	3.36	26.17

10 m for domains d03 and d04 were output by WRF as diagnostic variables. Model winds at 10 m agl for domain d05 were determined by interpolating between model grid point values at the surface and at the top of the first model layer at $\sim$ 12 m agl. Figure 3 shows wind-rose diagrams for case 1 on August 20 where output from model domains d03, d04 and d05 are compared to WBEA data at the location of Bertha Ganter–Fort McKay monitoring station. Wind directions for this case were from west and west-south-west during the simulation time, which is consistent with the observed WBEA wind directions. Model wind directions were within 20 to 30 degrees of the WBEA observational data. Model wind speeds were higher for all three domains compared to WBEA observational data for the locations of the two monitoring stations (with mean wind speed of 2.85 m/s): by 2 – 3 m/s for domain d03, by 3 – 4 m/s for domain d04, and by 4 – 6 m/s for domain d05. Note that the Large Eddy Simulation (LES) subgrid parameterization was used for d04 and d05 simulations. Model winds for these two domains, especially for d05, were highly variable over time and space. Figure 4 shows output from d04 and d05 compared to observational data from the two WBEA monitoring stations for wind, 2-m temperature and 2-m relative humidity for case 1. Comparisons for the other cases show similar results, with agreements within 5 °C for 2-m temperature, 1-25% for 2-m relative humidity, and 20-30 degree for wind direction. Similar to case 1, wind speeds were higher than WBEA winds by between 3 m/s to 6 m/s for case 3. Model wind speeds for case 2 were less than 1 m/s higher than WBEA observations with an average wind speed of 2.08 m/s. Evaluations for domain d05 against WBEA station Bertha Ganter – Fort McKay (AMS01) are summarized in Table 5 .

We note the following considerations when comparing model generated fields (e.g., wind) to WBEA observational data:

1. The lack of observational data from continuous monitoring stations for more spatial locations, especially closer to the centre of domain d05 (where CNRL is located) is a source of uncertainty. Note that the two available WBEA stations are located close to the southern boundary of domain d05, less than 200 model grid points from the boundary, as shown in Figure 2b. Model fields close to domain boundaries are highly impacted by the boundary conditions from the parent domain, and are usually not included in model output analysis. For this work, we considered a buffer zone of 100 grid
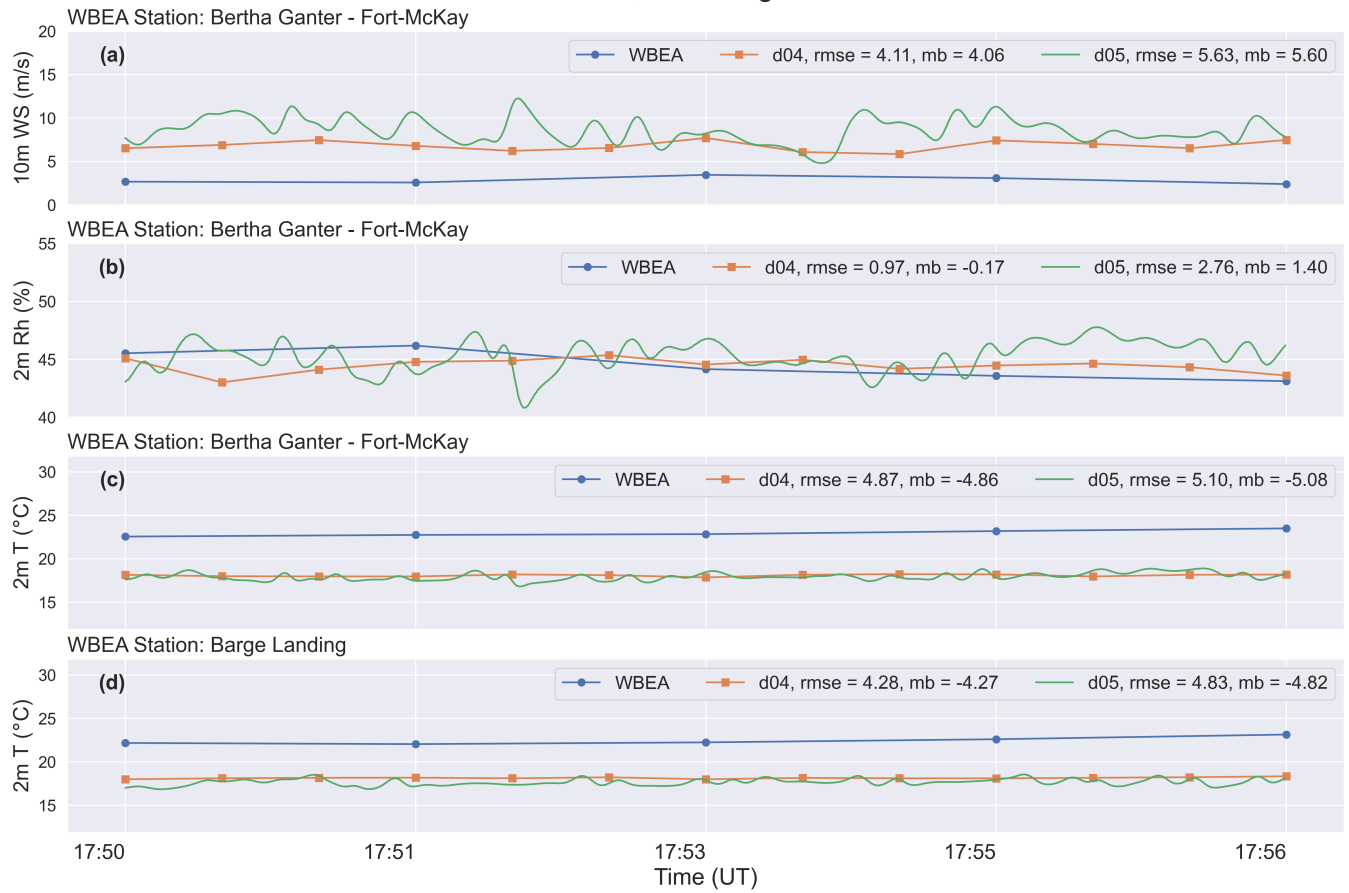
Figure 4. Case 1 model output from domains d04 and d05 for (a) 10-m wind speed, (b) 2-m relative humidity, and (c, d) 2-m temperature are evaluated against observational data from WBEA monitoring stations in terms of root-mean-square error (rmse) and mean bias (mb).

points on each side and excluded data from this zone in our analysis. We note that discrepancies between model fields and WBEA observational data are smaller for domains d03 and d04 compared to d05, where WBEA locations are well within the interior of the modelling domains (far from lateral boundaries).

2. The wind speeds in the NARR reanalysis data (at 31 km resolution) used as input for our simulations, were higher than WBEA observed values by 2-3 m/s for the region and the periods of interest. Consequently, the bias in NARR winds was carried through model nested simulations. If replicating the observed atmosphere is an objective of the modelling, it is recommended that input data (e.g., NARR reanalysis) to be adjusted to observations first.

3. Dynamical down-scaling of NARR reanalysis data from 31.25 km resolution to 50 m resolution with five nested domains and vertical grid refining, is another source of uncertainty. In concurrent grid nesting as used in this work, output from parent domain is interpolated to provide initial and boundary conditions for each respective nested domain. Horizontal,

vertical and temporal interpolation errors are therefore compounded with each nesting. This can result in biased wind fields as in Daniels et al. (2016), which is consistent with our results where d04 wind speeds were higher than d03 by about 1 m/s, and d05 winds were higher than d04 by about 1-2 m/s (see Table 4 for d04 vs. d05). While there may be a relationship between nesting and wind speed error, these results do not directly demonstrate a change in wind speed due to nesting.

4. The accuracy of subgrid scale LES parameterization in domains d04 and d05, is also a source of uncertainty. Liu et al. (2011) discussed concurrent nested modelling from synoptic scale to the LES scale with 4 domains. They demonstrate how simulated wind speeds differ by 2-5 m/s for the 4 domains, with weakest winds in the coarsest domain and stronger winds in the finest domain. Which is consistent with our results were wind speeds are biased high for the finest domain d05 compared to d04 and d03 by 1-4 m/s.

We also compared wind fields from domain d05 to aircraft observations during the JOSM 2013 campaign over the oil sands region for the same time periods as our model simulations. Figure 5 compares model wind speeds and directions for our three cases to aircraft observations for altitude levels of airborne measurements. Model data were averaged horizontally over domain d05 and the simulation time (Fig. 5), for comparison to aircraft data that were collected during 1-2 hours flight time over the oil sands region. Note that the near surface increase in wind speeds in Fig. 5 is the result of averaging over varying (complex) topography (see Figure S2 for instantaneous profiles at the location of the main CNRL stack). WBEA data at 10 m agl are also included on the figure for comparison. Horizontal bars on Fig. 5 show one standard deviation in model-generated fields over domain d05. Model wind fields (vertical profiles) overlap with aircraft observation within one standard deviation for the three cases. WBEA wind speeds are lower than both model and aircraft wind speeds. Note the high spatial heterogeneity in wind fields captured by both aircraft observations (Fig. 5, blue dots) and model simulations (Fig. 5, orange bars). Spatial (horizontal and vertical) variability in wind fields was larger for case 2 compared to the other two cases. We discuss in Section 3.5 how the conditions of case 2 resulted in weak advection of tracer mass and rendered this case unsuitable for mass-balance retrievals.

3.3 Plume Characteristics

In this section we briefly discuss plume behaviour for our three case studies with emphasis on case 1 as our main case. Continuous passive-tracer emissions for surface and stack sources were initiated simultaneously at different locations within the finest resolution modelling domain (d05), after a 30 min initial model spin-up time. Source locations, spatial extent, and release heights are provided in Table 2. Figure 6 shows tracer plumes for case 1 on 20 Aug 2013 at 17:35 UT, 2 hours and 5 minutes after the initial release. For the example shown, tracer plumes have propagated the downwind span of the modelling domain and reached the opposite lateral boundary. The mean direction of wind for the first 1.5 hour of the simulation for this case was from south west, which transitioned to winds from west and west-south-west in the following hours (Fig. 6). As mentioned before, we have discarded 100 grid points from the lateral boundaries of the domain and considered output data for the inner sub-domain in our analysis. The mass balance calculations discussed in Section 3.4 are for the period after 16:30UT (30 min after start up), as the addition of tracer mass through source emissions and removal via advective and turbulent fluxes
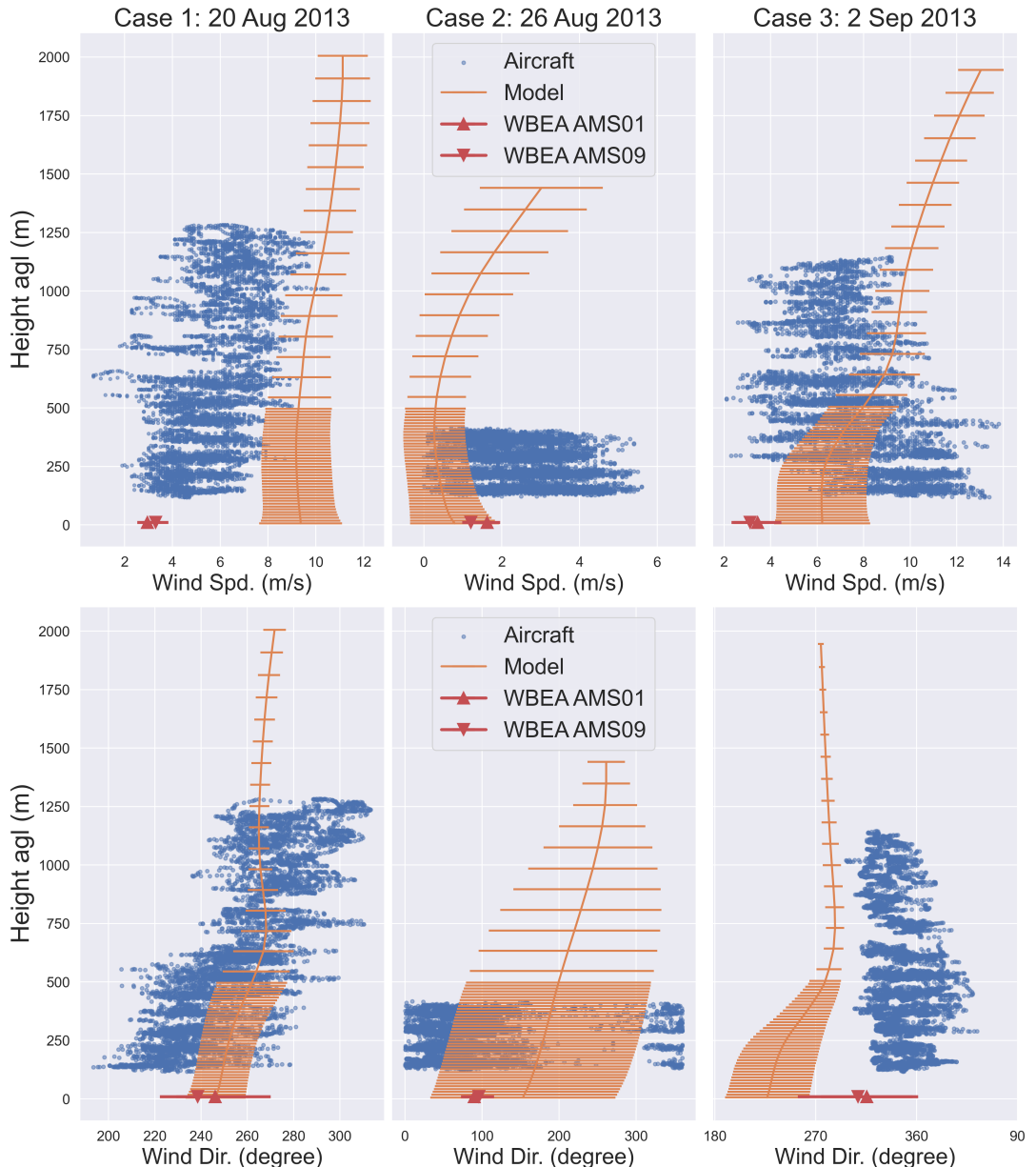
Figure 5. Model-generated wind fields (orange) compared to aircraft observations (blue dots) at several altitude levels during the JOSM 2013 airborne campaign, and WBEA observational data at 10 m agl (red triangles). Aircraft data were measured during the 1-2 hours Box Flight portion of the sampling period. Model data is averaged over domain d05 and the simulation time. Horizontal bars show one standard deviation in model wind fields (sum of standard deviations in space and time).

through the boundaries of the control volume (box) have reached a mass-balance and a relative steady-state by this point in the simulation time.
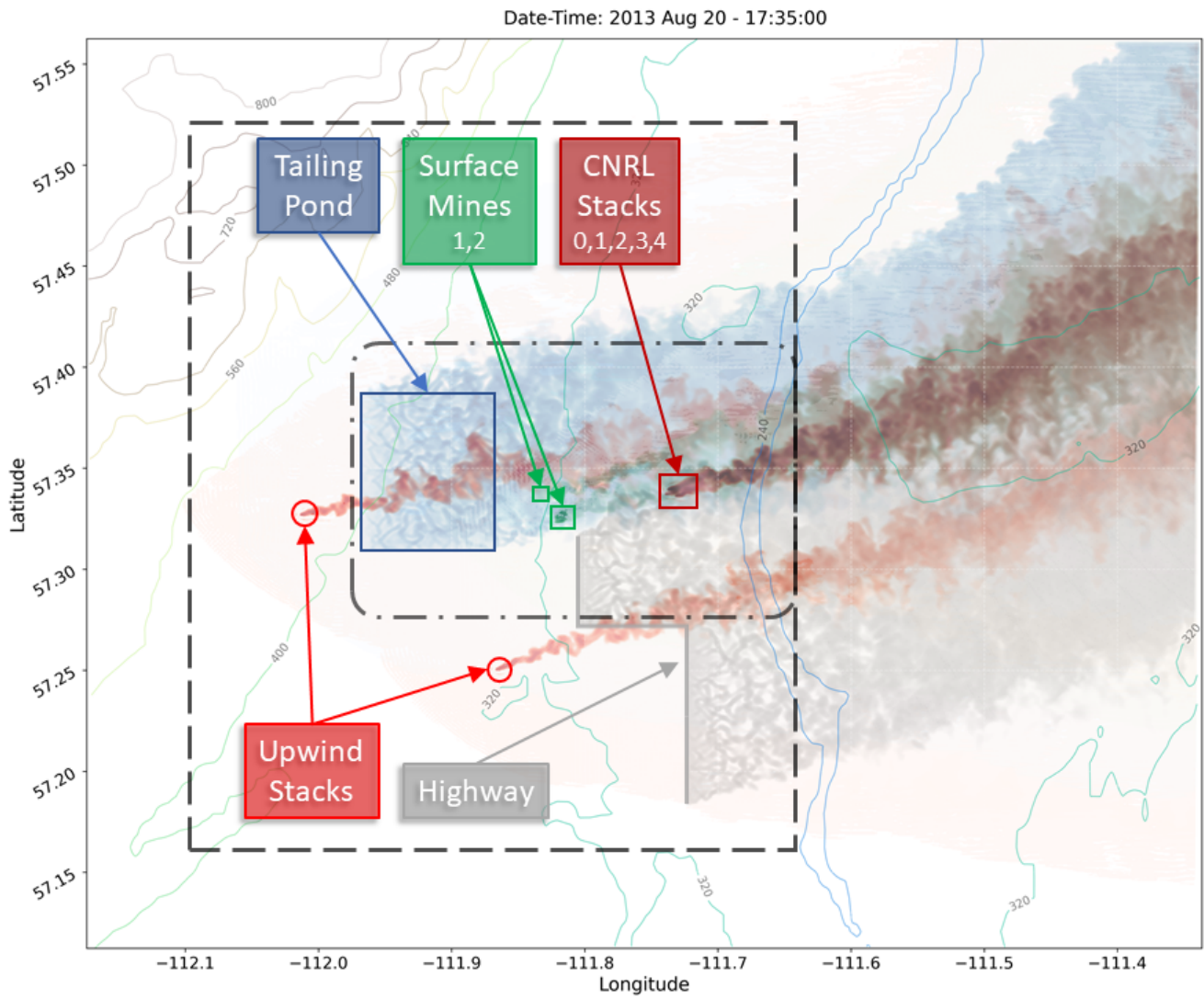
Figure 6. Top view of the modelling domain (d05) and the location of tracer emission sources are shown. Sources include a big area source (Pond), a multi-segment line source (Highway), two small area sources (Mines 1, 2), five CNRL stacks 0-4 and two upwind point sources (west and south). Emission plumes from Pond are shown in blue, Highway in gray, Mines in green and stack/point sources in red. Colour darkness is proportional to log of column total tracer mass. Two control volumes (dark dashed boxes) for 4D mass-balance calculations are shown, one enclosing all the emission sources and the other marking the boundaries of the CNRL facility (the smaller box) and only including within facility sources.

Tracer amounts were advected at different vertical levels and flow regimes. Flow was different at other vertical levels. For instance, surface emissions from MINE1 and MINE2 (Fig. S4 top right panel) were advected in slower air flows and covered less downwind range during the same time period compared to stack (elevated) emissions CNRL0-4 (Fig. S4 top left panel).
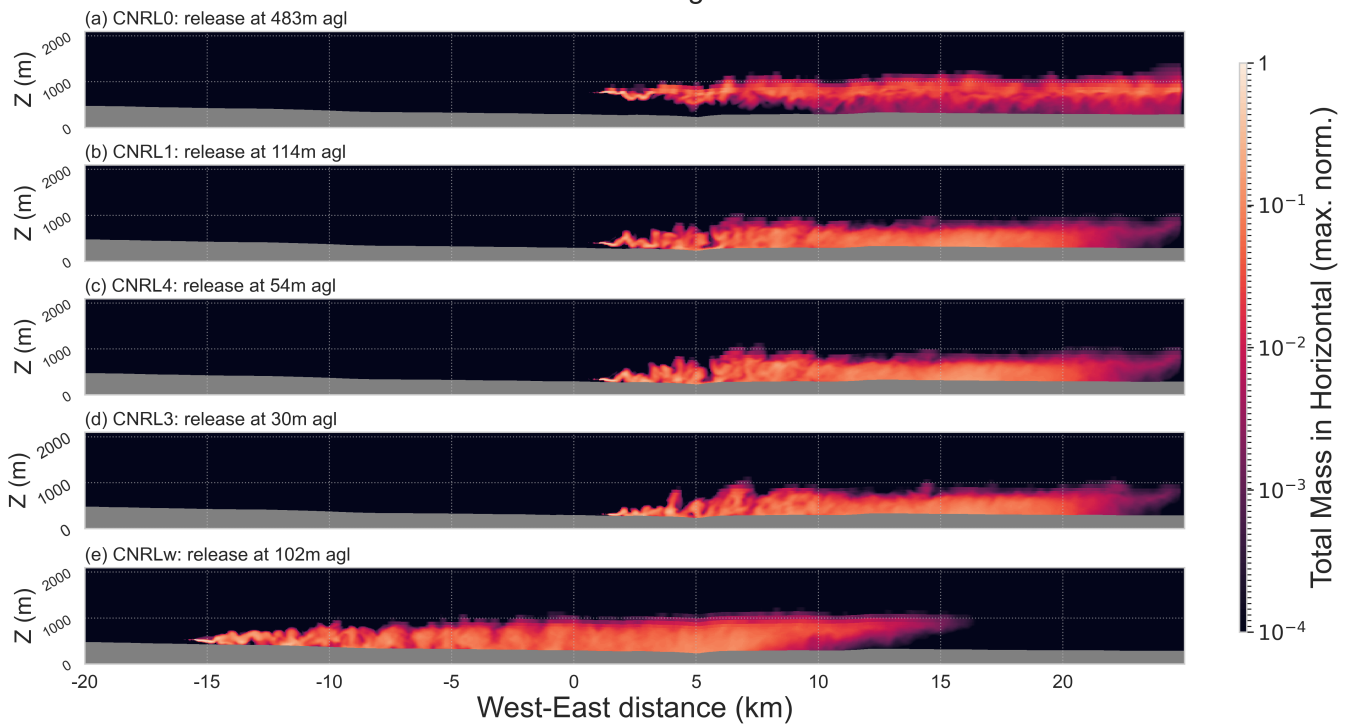
Figure 7. Domain d05 west-east vertical cross-section for case 1 on 20 August 2013. Vertical cross-section of tracer plumes from stack/point emission sources are shown. Release height above ground is indicated for each source. Data shown is the tracer amount summed in the horizontal level and normalized to the maximum value for each source. The origin for west-east distance in km is at domain centre.

Figure 7 shows a west-east vertical cross-section of the modelling domain, with tracer plumes from select stack/point emission sources. Advection in west-east orientation is unidirectional at all vertical layers as can be seen in Fig. 7. The plume centre-line for CNRL0 emissions remains near the initial release height, while mixing in the vertical as it is advected downwind. CNRL1-4 emissions, although released at different heights above ground (by a few tens of meters), show similar vertical mixing profiles along the downwind advection path. Emissions from CNRL1-4, mixed to the ground surface within the 5 km range and assumed a near uniform vertical mixing beyond 15 km downwind distance. Note how plumes from these sources interact with the Athabasca river basin at the 5 km distance. There is an apparent discontinuity in tracer concentrations beyond which mixing in the vertical is intensified. This is likely due to different surface fluxes over the river and the ground on either side with stronger updrafts. This interaction is less visible in CNRLw plume which is relatively well mixed by 5 km distance, but it can be seen that the vertical mixing becomes more uniform on the other side of the river for this plume.

Wind and therefore transport in the south-north direction were weaker than the the transport in the west-east direction. There was also a strong vertical shear in south-north wind (V). See Appendix Figure C1 for meteorological vertical profiles for this case. While all tracer plumes for release heights of 30 m to 114 m agl were advected north, CNRL0 at 483 m agl was

advected south (Fig. S5 top panel). Similar atmospheric processes governed the dispersion and transport of tracer plumes from the surface emission sources (see Figure S6).

WRF model simulations for case 2 for the period during 26 August 2013 started at 18UT. As mentioned before, the JOSM box flight (see Section 2.1) for this day was rejected for emission rate calculations due to low and variable wind speeds as reported in Fathi et al. (2021). This case is referred to as "rejected" throughout this work. We recreated the meteorological and tracer transport conditions on this day with our super-resolution simulations, which are presented here as an example of unsuitable conditions for top-down retrieval. For this case, tracer emissions from various sources were initiated at 18:30UT. During the period between 19UT to 21UT, wind fields over the region of interest were highly variable (spatially) with very low wind speeds (Figure S7). For case 2, wind speeds at a height of 10 m agl were less than 5 m/s over the modelling domain. The mean wind direction was towards the south and south-west near the ground, transitioning towards the south-east up to 1000 m agl, and towards east and north-east above 1000 m agl. The south-north wind component V ranged from -1 m/s to 1.5 m/s in the vertical, with the west-east wind component U ranging from -0.5 m/s near the ground surface to 7.5 m/s up to 2500 m agl. See Appendix Figure C2 for meteorological vertical profiles for this case. The weak advection and the strong vertical wind shear resulted in tracer plumes being transported for only a few kilometres in the horizontal and mainly staying within the boundaries of the CNRL facility (Fig. S7).

Unstable atmospheric conditions persisted during the simulation period over the region of interest for case 2. Gradient Richardson number (Ri) values, which is a measure for atmospheric dynamic stability (Fathi et al., 2021), were below the critical value of $Ri_c = 0.25$ up to 400 m agl. Ri values below 0.25 correspond to unstable conditions in the atmosphere (AMS, 2022). Consequently, tracer plumes from emission sources mixed in the vertical up to 2000 m during the simulation time. Similar meteorological and atmospheric conditions were observed during the the JOSM 2013 field campaign during the same period. These conditions were also simulated using Environment and Climate Change Canada's (ECCC) air-quality model GEM-MACH at 2.5 km resolution. Our super-resolution (50 m) WRF model simulations were also successful in recreating the conditions on 26 August 2013 over CNRL. See (section 4.2, Fathi et al., 2021) for detailed discussions on how low and variable wind and unstable conditions affect the atmospheric transport of tracer plumes for this case.

Case 3 model simulations at super-resolutions for the period during 2 September 2013 started at 15UT. Tracer emissions were initiated at 15:30UT. Atmospheric conditions during this case were fairly stable, with Gradient Richardson number Ri exceeding the critical values $Ri_c = 0.25$ (indicating atmospheric dynamic stability) below 100 m above ground level (agl). Wind speeds were higher for this case compared to the other cases with west-east wind component U ranging from 5 m/s near ground surface to 15 m/s up to 2000 m agl. The south-north component of the wind V was about 5 m/s near the surface, with a strong shear in the vertical transitioning towards south at about 500 m agl. See Figure C3 for meteorological vertical profiles during the time period of this case. Similar to case 1, the mean direction of transport was towards east and north-east, but with a stronger northward component compared to case 1 (see Figure S8)

Average inversion heights Z_i (inferred from potential temperature θ profiles) for the three cases are marked with dashed lines in Figures C1, C2, and C3. Z_i for cases 1 and 3 was between 300-400 m agl , placing the tracer sources (all except CNRL0) within the atmospheric boundary layer (ABL) where turbulent mixing plays a dominant role in modifying the vertical structure
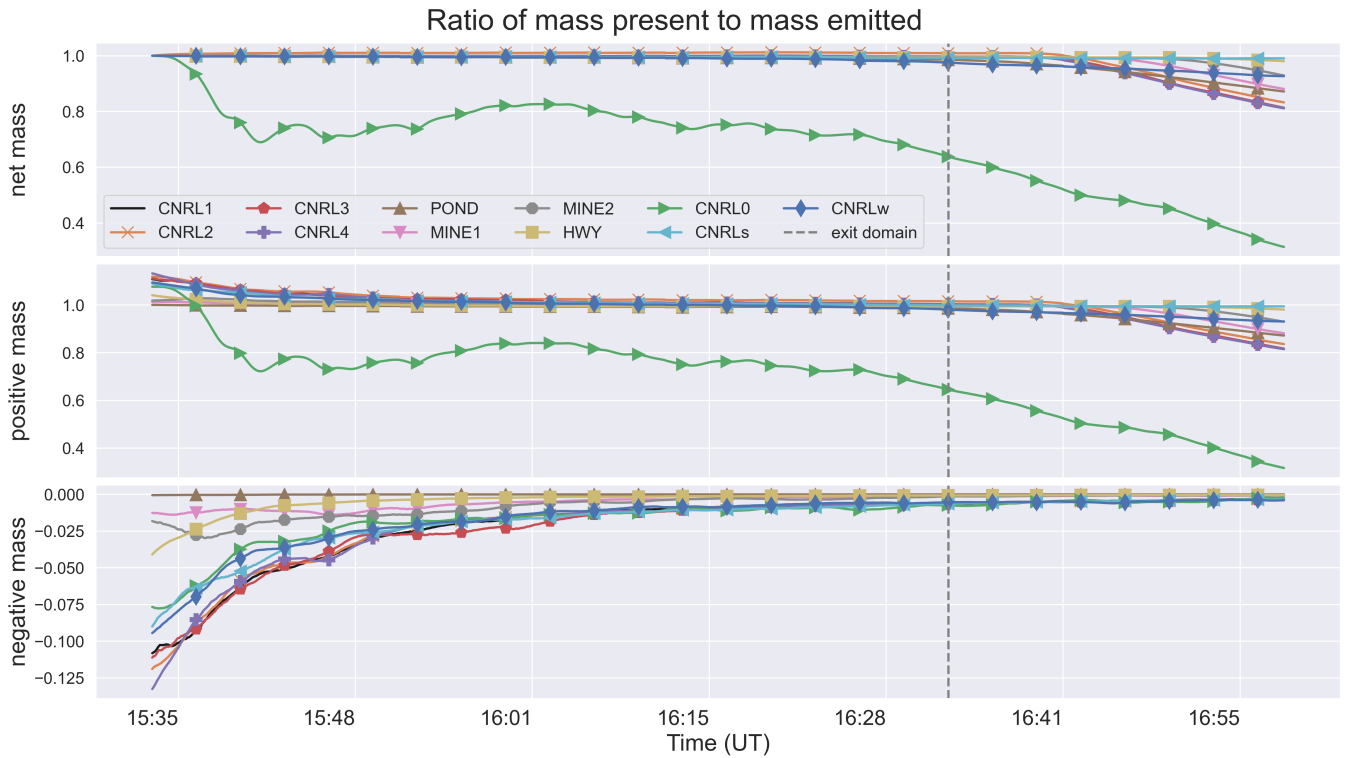
Figure 8. The ratio of tracer mass present within the modelling domain to mass emitted over simulation time after the start of tracer release. Time series are separated into positive and negative mass in the bottom two panels. Tracer mass remains conserved over time, with the exception of CNRL0. Note that the drop in present-to-emitted mass ratio beyond 16:30UT, marked by the vertical dashed line, is due to tracer mass exiting through domain boundaries and not a violation of mass conservation.

of the atmosphere including tracer concentrations. As a result tracer amounts released from these sources (at different heights) were mixed quickly in the vertical extent of the ABL within the 10 km downwind distance resulting in similar uniform vertical profiles (Fig. 7). For cases 1 and 3 the CNRL0 release height at 483 m agl was above Z_i, where turbulent mixing is suppressed by the negatively buoyant atmosphere in the stably stratified inversion layer. Which confined the dispersion of CNRL0 tracer amounts within a smaller vertical extent and detached from the ground surface up to 10 km downwind distance (see Fig. 7). For case 2, Z_i was between 1400-1500 m agl, placing all source including CNRL0 well within the ABL and resulting in similar vertical mixing for tracers released at different heights from ground surface up to 483 m agl and in the downwind distance (see Figure S9).

3.4 Model Global Tracer Mass Conservation and Emission Rate Calculation

In this section we evaluate the conservation of tracer mass within domain d05. As discussed in Section 2.2, in our simulations we used a positive-definite transport scheme combined with a sixth order diffusion scheme. Negative up-gradient diffusion flux

near sharp concentration gradients resulted in partial creation of erroneous mass within the modelling domain. Positive flux and monotonicity can be enforced in the model by setting negative fluxes to zero, however this is not mass conserved (see Figure S10). Therefore we configured our simulation using the diffusion scheme without the monotonic option. We investigated the tracer mass budget within domain d05 by integrating over the entire domain at each model output time-step (Eq. 2). Figure 8 shows the ratios of mass present in the modelling domain at each timestamp to the total mass emitted up to that point. The ratios are for the eleven emission scenarios for the first hour after tracer release was initiated. The net mass present within the modelling domain is separated into negative and positive mass. Time-series are shown as the ratio of mass present in the domain to mass emitted (normalized) for each emission source. Initially up to 14% negative mass (Fig. 8, bottom panel) is created within the domain which is offset by about the same amount of excess positive mass creation (Fig. 8, middle panel). The net mass (Fig. 8, top panel) is conserved as the negative and the excess positive mass cancel out. The creation of negative mass is reduced over simulation time until it falls below 2% after about 30 min simulation time. The creation of negative mass is likely due to sharp gradients in tracer mass immediately after the initial release, which are concentrated mostly upwind of the emission sources. As tracer mass is advected and dispersed over several grid points, the gradient is smoothed out and negative mass creation becomes less pronounced. The present-to-emitted mass ratio for 10 out of 11 sources are conserved and remain equal to unity up to about 16:30UT when they reach the domain boundaries and are removed from the modelling domain (Fig. 8, top panel). The exception is CNRL0, which does not keep up with the emissions and, except for a few minutes after the initial release, is always less than one. The mass present in the domain (not normalized) increases initially and later plateaus (approaching an asymptote) as plumes start exiting through domain boundaries at rates less than or equal to source emission rates. Similarly, the decrease in present-to-emitted mass ratio in Fig. 8 (marked by a vertical line) is a result of tracer mass exiting through domain boundaries at rates less than or equal to source emission rates (and not a violation of model mass conservation).

Figure 9 shows temporal rate of change in tracer mass for each emission scenario, normalized to model input emission rate (MIE). This rate of change was calculated by differentiating the domain mass time-series shown in Fig. 8 according to Eq. 3, which is equivalent to the storage rate term for the entire domain ($S_{C,d05}$). The net rate of change (top panel) is separated into rates for positive and negative mass in the bottom two panels, for each tracer case. The rate of creation of negative mass oscillates between -10% and 5% and is damped over time. This is offset by the creation of excess positive mass, resulting in net mass conservation over the modelling domain (an artifact of the model transport scheme). For tracer mass to be conserved, the net rate of change over the entire domain must be equal to model input emission rate for the time period before tracer plumes start exiting through domain boundaries (before about 16:30UT for most tracers as shown in Fig. 9). Tracer mass at domain boundaries was set to zero (boundary condition). As plumes reached the boundaries the tracer mass was removed from the domain (at different times for each tracer depending on the transport speed and source proximity to the boundaries), hence the drop in $S_{C,d05}$ as shown in Fig. 9. This was true for all emission scenarios as can be seen from Fig. 9 top panel. The $S_{C,d05}$ time-series for ten out of eleven sources were at MIE level, indicating mass conservation for these cases. The only exception was CNRL0 for which $S_{C,d05}$ oscillated around MIE without converging. It is evident from Figures 8 and 9 that CNRL0 mass was not conserved.
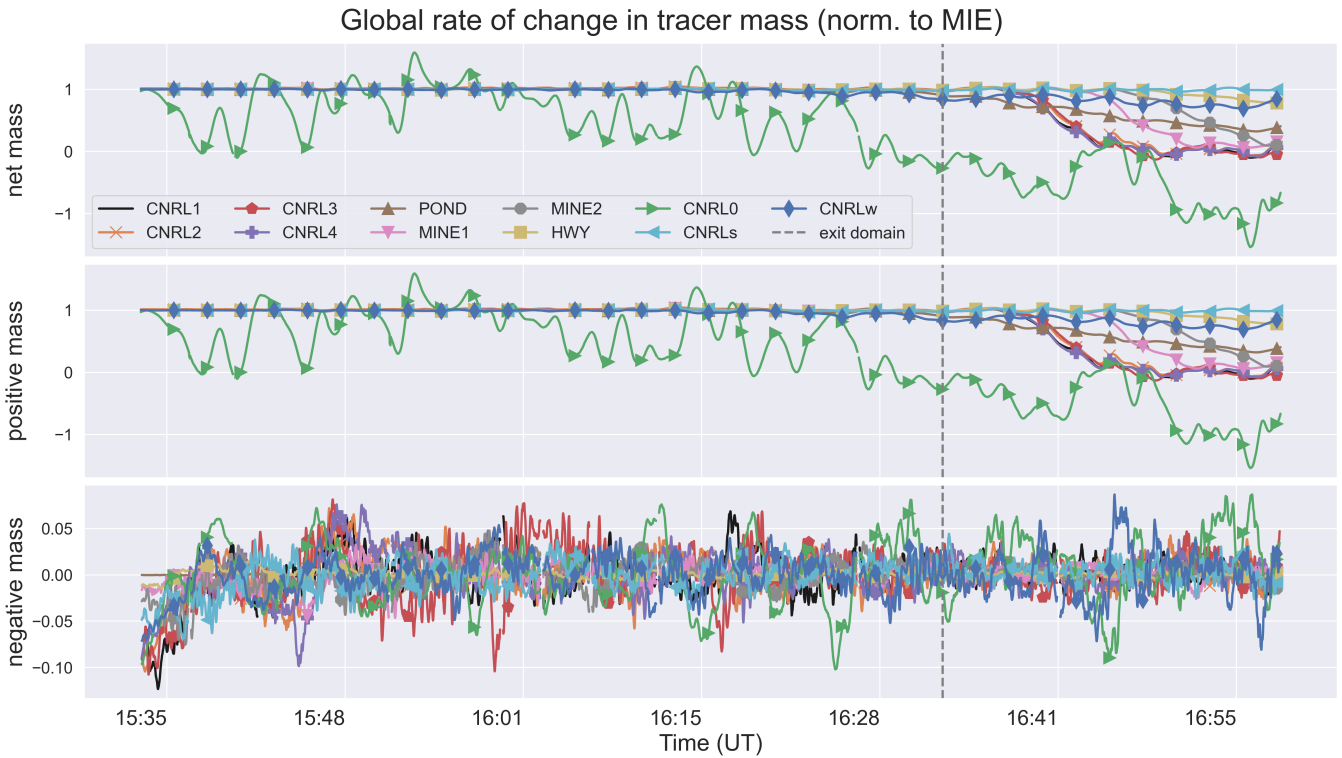
Figure 9. Temporal rate of change in tracer mass for the entire domain $S_{C,d05}$ is shown. Time series are normalized to model input emission (MIE) rates. The net rate of change (top panel) is separated into rates for positive and negative mass in the bottom two panels. The creation of negative mass is offset by creation of excess positive mass. Rate of change in tracer mass match MIE (conserved) for all except one emission source (CNRL0).

For the case of CNRL0, tracer release height was at the model vertical level where model resolution (vertical) transitions from model layer thickness of about 12 m to progressively increasing thicknesses (and decreasing resolutions). Transport
465 (advection and diffusion) of tracer amounts between model vertical layers of varying resolutions, likely intensified erroneous and unbalanced (by excess positive mass) creation of negative mass (both in magnitude and spatial location). While the positive-definite transport scheme ensures positive and conserved advection of tracers, the negative up-gradient diffusion can still create erroneous mass. Our results suggest that this is intensified on a non-uniform grid (varying grid size). However, more in-depth investigation (beyond the scope of this paper) is required to confirm such effects. Table 6 lists statistics for the first hour of
470 tracer emissions (before exiting through domain boundaries) for all emission scenarios. The temporal means (μ) and standard deviations (σ) are indicated for the normalized rates ($S_{C,d05}$) shown in Fig. 9. As mentioned before, CNRL0 is the only non-conservative case with a mean value of 0.69 and standard deviation of 0.39. Therefore, in this paper and in (Fathi, 2022) we discuss CNRL0 mainly in terms of plume behaviour rather than a conserved quantity in mass-balance calculations. The mean normalized rates for CNRL2 and CNRLw were within 2% and 1% of MIE, respectively. For the remaining 8 out 11 cases, the

475 mean normalized rates were equal to 1.00 (strong agreement with model input emission rates). These results apply to all three case studies within 2-4%.

Table 6. Normalized (to MIE) rates of change in tracer mass for all emission scenarios are shown. Mean rates are given for net, positive (+) and negative (−) mass. Standard deviations are also provided. Rates agree with model input emissions within 2% for 10 out 11 tracers (conserved).

Tracer ID	Temporal Mean (μ)			Standard Deviation (σ)		
	net	+	−	net	+	−
CNRL1	1.00	1.00	0.00	0.07	0.07	0.03
CNRL2	1.02	1.00	0.00	0.07	0.07	0.03
CNRL3	1.00	1.00	0.00	0.07	0.07	0.04
CNRL4	1.00	1.00	0.00	0.07	0.07	0.03
POND	1.00	1.00	0.00	0.07	0.07	0.00
MINE1	1.00	1.00	0.00	0.07	0.07	0.02
MINE2	1.00	1.00	0.00	0.07	0.07	0.03
HWY	1.00	1.00	0.00	0.07	0.07	0.01
CNRLs	1.00	1.00	0.00	0.07	0.07	0.03
CNRLw	0.99	0.99	0.00	0.07	0.07	0.03
CNRL0	0.69	0.69	0.00	0.39	0.39	0.03

3.5 Local Mass Conservation and Mass-balance Analysis

Results in Table 6 indicate global (over the entire modelling domain) mass conservation for 10 out 11 emission cases. We further evaluated model local mass conservation through mass-balance and flux calculations in order to assess the model's ability to

480 be used for accurate mass-balance assessment. A control volume enclosing all the emission sources, with the downwind wall at a 5 km distance from the main CNRL stacks, was considered (large rectangle in Fig. 6). We conducted 4D mass-balance calculations using this control volume for all case studies, to evaluate the performance of model simulations in the context of local mass conservation and transport of tracer amounts within a sub-domain (control volume). The mass-balance calculations for this portion of our analysis were conducted for the period between 1 to 2 hours after the tracer release started, well after

485 plumes crossed the box (control volume) walls.

Mass-balance calculations were done according to Eq. 6. The net flux out term $F_{C,out}$ was calculated using the instantaneous fields (e.g., wind speed, tracer concentrations) along top and lateral boundaries of the control volume. $F_{C,out}$ includes horizontal ($F_{C,H}$, $F_{C,HT}$) and vertical ($F_{C,V}$, $F_{C,VT}$) advective and turbulent fluxes across box walls. The rate of mass storage/release S_C within the control volume (box) at each model output time-step (1 second) was calculated by integrating over the entire

490 volume of the box and differentiating with respect to time. Source emission rates E_C were calculated as the sum of $F_{C,out}$ and S_C and were compared to model input emission rates (MIE). Contributions (absolute value) of different terms are shown in
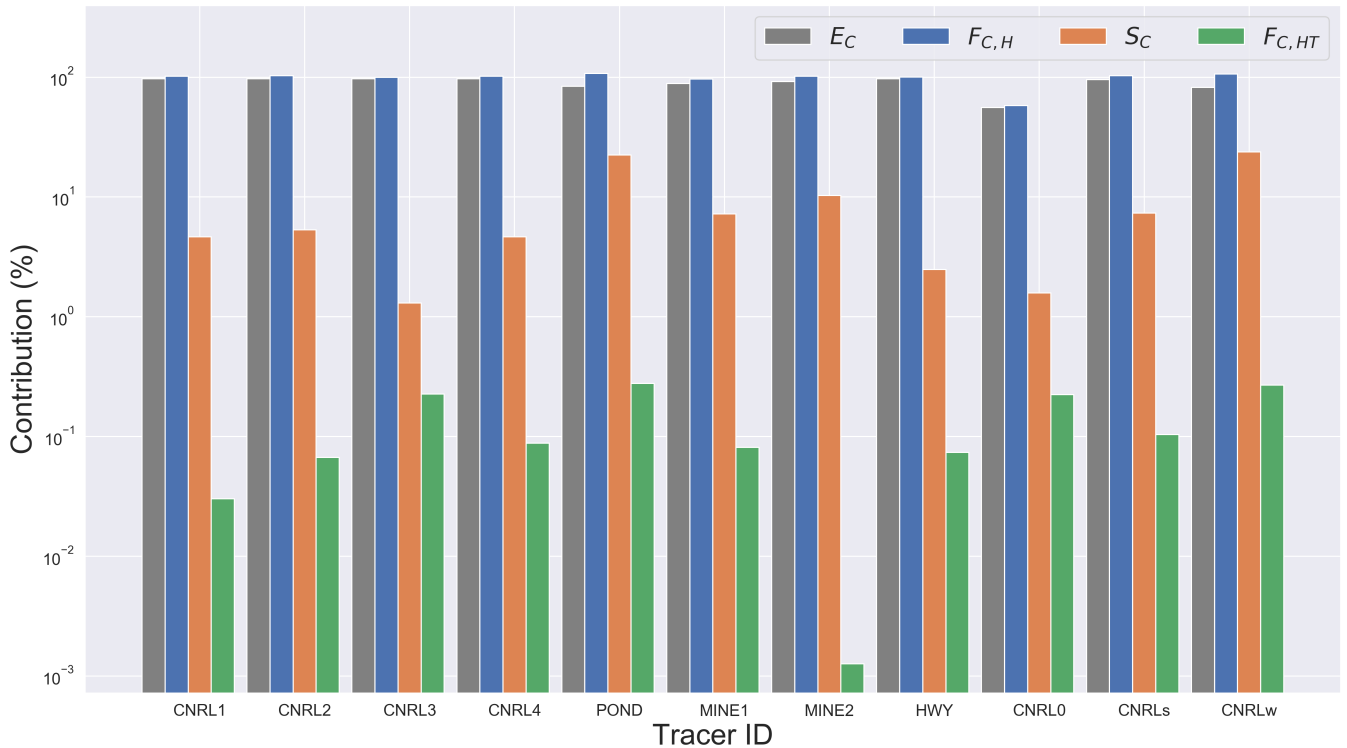
Figure 10. Normalized (to model input emissions - MIE) retrieved emission rates for tracer emission scenarios of case 1. Emission rates (E_C) were calculated using the mass-balance equation Eq. 6 and the control volume shown in Fig. 6. The breakdown (%) of contributing terms are shown as absolute values, see Table 7 for the actual values. The vertical axis is in log scale. Refer to Table 2 for source specifications.

Figure 10 for case 1. The main contribution came from the horizontal advective flux, along with significant contributions from the storage rate term S_C. The horizontal turbulent flux contributed between -0.3% to 2.3% for the three cases. Contributions from vertical fluxes were negligible as the box top was chosen at a height of over 4 km agl, well above the mixing layer height at about 2-3 km agl. The breakdown of contributing terms for the three cases are summarized in Table 7.

For case 1, mass-balance estimates were within 4% of model input emission rates (MIE) for 10 out of 11 tracers (see Table 7). Estimates for the (globally) non-conservative tracer CNRL 0 were biased low by 51%. Estimated emission rates for all the other emission scenarios were in over 96% agreement with MIE. Contributions from the storage rate term S_C were negative (release of mass from the control volume) for ten emission scenarios and ranged between 1% to 30%. The contribution of S_C for MINE2 was positive (storage of mass in the control volume) and about 4%. $F_{C,H}$ contributions were positive and ranged between 51% to 130%, which were offset by negative S_C contributions. Our results with GEM-MACH model simulations in Fathi et al. (2021) for SO$_2$ emissions (stack/point source) for the same time period, were very similar (97% $F_{C,H}$ and 3% S_C) to stack emissions simulated here with WRF at super-resolution. The model based study by Panitz et al. (2002) attributes 85%

Table 7. Source emission rates (E_C) determined by performing mass-balance calculations on model output data, evaluated against model input emissions (MIE) for the three cases. Results are shown as normalized mean bias (nmb) in %. Contribution of three main terms in the mass-balance equation are shown, normalized to MIE (%). Values less than 0.1% are indicated with ϵ.

| | Case 1 | | | | Case 2 | | | | Case 3 | | | |
| | E_C | Contributions (%) | | | E_C | Contributions (%) | | | E_C | Contributions (%) | | |
Tracer ID	nmb (%)	S_C	$F_{C,H}$	$F_{C,HT}$	nmb (%)	S_C	$F_{C,H}$	$F_{C,HT}$	nmb (%)	S_C	$F_{C,H}$	$F_{C,HT}$
CNRL1	-4.0	-2.9	99.2	-0.3	-1.7	97.7	0.7	ϵ	1.5	-27.5	127.3	1.7
CNRL2	-3.2	-4.4	101.2	-0.1	3.3	102.7	0.6	ϵ	1.3	-26.6	126.3	1.5
CNRL3	-3.7	-3.7	100.0	-0.1	-2.6	94.6	2.8	ϵ	1.0	-27.5	127.1	1.4
CNRL4	-3.8	-3.9	100.2	-0.1	-3.9	92.4	3.6	ϵ	1.4	-27.2	127.0	1.6
POND	-4.4	-10.9	106.2	0.3	-4.2	92.0	3.8	ϵ	-3.8	15.4	80.6	0.2
MINE1	-0.4	-8.6	108.4	-0.2	-1.9	96.1	2.0	ϵ	-1.2	5.1	93.3	0.3
MINE2	3.9	-3.0	107.3	-0.3	1.6	97.4	4.2	ϵ	-0.9	5.6	92.7	0.7
HWY	-1.2	-3.0	101.8	ϵ	-4.8	90.3	4.7	0.2	-0.6	-19.2	118.3	0.3
CNRLs	-3.8	-8.7	105.0	ϵ	-4.9	90.7	4.3	ϵ	-1.4	10.0	88.0	0.6
CNRLw	-3.8	-29.8	126.2	-0.1	3.1	88.9	11.9	2.3	-3.1	72.1	24.6	0.1
CNRL0	-50.7	-1.3	50.9	-0.3	-49.5	49.7	0.8	ϵ	-54.1	5.7	40.6	-0.4

to 95% of the emissions to advective fluxes (for SO$_2$ and CO), which is also consistent with our estimates. Our results here

505 with WRF (LES) simulations are within the range of previous model studies.

Mass-balance estimates for case 2 were within 5% of MIE for the ten emission scenarios (Tables 7). Estimates for CNRL0 were biased low, similar to case 1, by about 50% (not conserved). For this case, where wind speeds were very low and spatially heterogeneous, the tracer amounts were mainly stalled within the control volume over the simulation time. Consequently, the storage rate term S_C was the dominant term with contributions (positive) ranging from 89% to 103%. The horizontal

510 advective flux $F_{C,H}$ contributed to the mass-balance equation between 0.6% to 12%. The contributions from vertical and turbulent fluxes were less than 1%, except for CNRLw with 2.3% contribution. Our estimates for SO$_2$ emission rates for CNRL with GEM-MACH simulations in Fathi et al. (2021) showed similar large storage levels. We note that conditions of weak advection were also observed during JOSM 2013 airborne campaign for the period of case 2 on 26 August 2013 (see Fig. 5), which resulted in negligible estimated emission rates based on flux calculations alone (i.e., not accounting for

515 storage). As a result of such conditions, the emission estimation flights for this time period were not included (rejected) for top-down retrievals in the post campaign studies. Note that GEM-MACH model simulations at 2.5 km resolution for the same case (26 August 2013), predicted a storage contribution of only 43% (Fathi et al., 2021). Whereas, WRF super-resolution simulations in this work predicted a contribution of $\geq$ 89%. While both modelling setups replicated the same meteorological (advection) conditions, the relatively coarser resolution of GEM-MACH simulations resulted in larger computational (grid)

520 diffusion and consequently larger downwind dispersion of tracer amounts (and larger predicted horizontal mass flux). This in part demonstrates the benefits of employing super-resolution over high-resolution modelling. The WRF super-resolution simulations in this work were successful in closely replicating the observed weak advection conditions and GEM-MACH predicted $F_{C,H} < 20\%$ for the same period (Fathi et al., 2021) , but at a higher spatio-temporal resolution.

Mass-balance estimates for case 3 were similar to estimates for case 1, with over 96% agreement with model input emissions
525 (MIE) for the ten emission scenarios. Similar to case 1 and case 2, CNRL0 estimates were biased low (at 54%). For case 3, the contribution of the storage rate term S_C ranged between -27.5% to 72.1%. The horizontal advective flux $F_{C,H}$ contributed between 25% to 127% to the mass-balance equation. The horizontal turbulent flux contributed between -0.4% to 1.7%. Similar to case 1 and case 2, contribution of vertical fluxes were negligible.

As can be seen from Table 7, our mass-balance estimates for the three cases were within 5% of model input emissions (MIE).
530 Estimates were partially affected by local mass deficit/surplus for these cases. As discussed at the beginning of this section, the turbulent diffusion step in our WRF model setup created erroneous negative mass (locally) within the modelling domain. The negative mass was mainly created near the emission source (upwind) and at plume edges, as indicated in Figure 11. The advection of positive/negative mass passed the box-downwind-wall (vertical dashed line in Fig. 11) was not always balanced, due to different spatial distributions for positive and negative amounts. Fig. 11 shows three snapshots at 5 min intervals for
535 tracer MINE1 during the final hour of case 1. As indicated on the figure, during this time period 98% of the domain total negative mass remained inside the control volume along with only about 43% of the domain total positive mass. This resulted in a mismatch between the negative mass and the excess positive mass and the consequent mass emission rate underestimations for this and similar cases. Estimates were also partially affected by the changing vertical grid spacing for upper model layers, for tracer amounts mixing to higher altitudes (> 500 m). This is similar to mass loss for CNRL0 emissions, but to a much
540 lesser extent. We conclude that all three cases (with ten emission scenarios) were globally (on the entire modelling domain) and locally (control volume) mass conserved within 4% and 5% of MIE , respectively.

4   Conclusions

We developed and implemented super-resolution (< 100 m) model simulations employing the WRF-ARW atmospheric modelling system. We used NARR reanalysis data at 31 km resolution as initial and boundary conditions for our coarsest domain at
545 the same resolution. Dynamical down-scaling of reanalysis data was done through numerical model nesting with five domains from 31 km to 50 m at the finest resolution domain over the oil sands facility CNRL. We chose our model simulation times and locations from three emission rate retrieval flights during the JOSM field campaign in August and September 2013. We performed model simulations for three days in August and September, representing different meteorological conditions. Model simulations for the finest resolution domain were conducted using Large Eddy Simulation (LES) sub-grid parameterization.
550 The main objective was to model the state of the atmosphere at high enough resolution to simulate atmospheric dynamical processes at spatial and temporal scales of airborne measurements, while ensuring local and global mass conservation. Model output data from our simulation cases were evaluated against historical observational data from two WBEA monitoring sta-
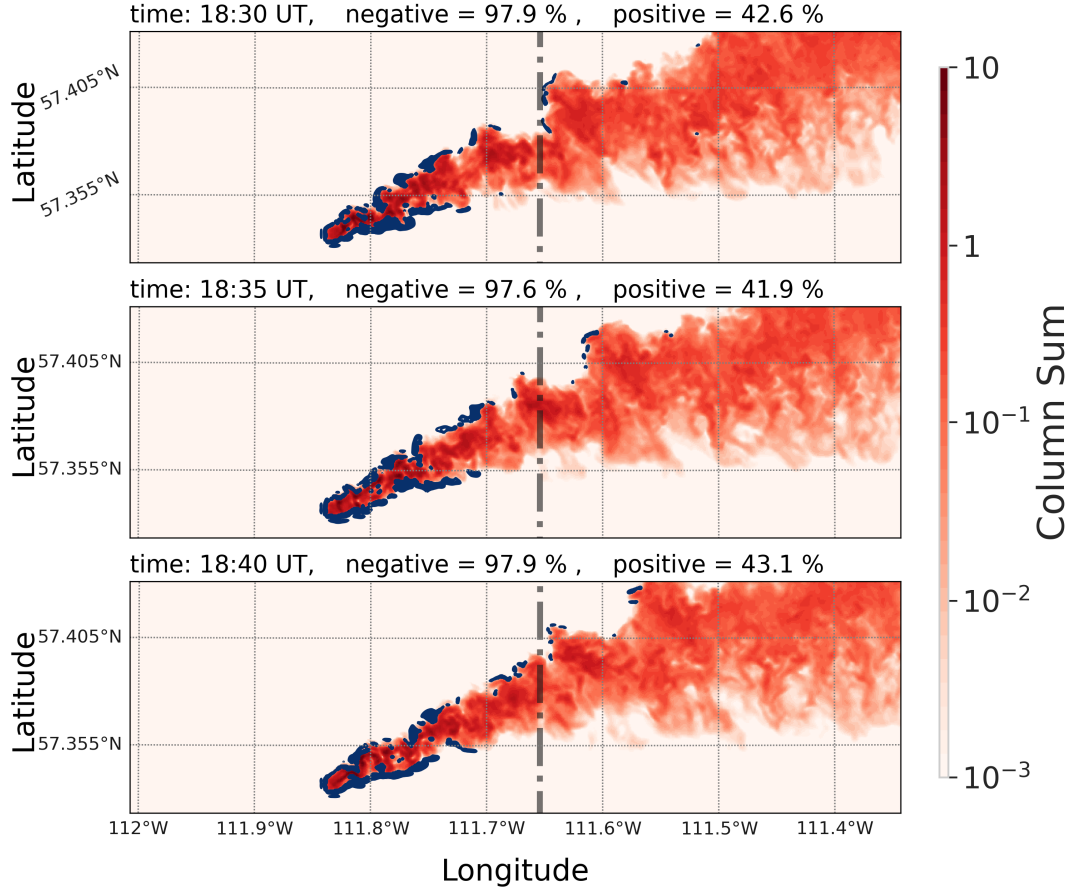
Figure 11. Three panel snapshot of MINE1 plume during case 1 at 5 min intervals. Note that the erroneous negative mass creation (blue contours) is concentrated upwind of the emission source and on plume edges. Consequently, 98% of the domain total negative mass was located within the control volume along with only 43% of total positive mass (red). The vertical dashed line shows the location of control volume downwind wall.

tions, as well as aircraft observations during JOSM 2013 campaign for the same locations and time periods. Model output fields showed good agreement with observational data within 5% in terms of 2-m temperature, 2-m relative humidity, and 10-
555 m winds. General wind directions generated by the super-resolution model were within 20 to 30 degrees of the observational data. Model wind speeds were in agreement with aircraft observations within one standard deviation.

We modified WRF model dynamical solver source code to simulate passive tracer emissions within the finest modelling domain, centred over the CNRL facility. Our case simulations included eleven different emission scenarios with stack/point and surface/area sources. Continuous emissions were simulated for time periods of 2-3 hours during three different days.
560 We evaluated the atmospheric dispersion and transport of tracer plumes from the eleven emission scenarios under different

meteorological conditions. Unstable atmospheric conditions, low wind speeds, and strong vertical wind shear during our case study on 26 August 2013 resulted in weak advection of tracer plumes during the simulation time. During case studies on 20 August and 2 September, atmospheric conditions were relatively more stable with higher wind speeds of about 5-15 m/s. Tracer plumes from emission sources were advected mainly towards east and north-east for these two cases. Similar conditions have been observed during the JOSM 2013 field campaign for the same time periods and locations as our three case studies.

We evaluated the performance of our model simulations in terms of global (over the entire domain) mass conservation. For one case out of eleven, creation of erroneous mass by the model transport step resulted in loss of tracer mass. For this emission case, tracer release was placed at the model vertical level where model vertical resolution transitions from the super-resolution of about 10 m to progressively coarser resolutions. Our results suggest that the unbalanced creation of erroneous mass at sharp concentration gradients, such as at the vicinity of point sources, is intensified on an irregular grid (an artifact of model dispersion). However, more investigation with longer simulation times (beyond the scope of this paper) are required to further investigate such effects. Small negative diffusive fluxes and the use of the positive-definite re-normalization scheme in our modelling setup prevented nonphysical effects (e.g., negative mass creation) for 10 out 11 emission sources (assigned on a regular grid). The rate of change for tracer mass was calculated by integrating over the entire modelling domain and differentiating with respect to time. Results were within 2-4% of model input emissions (MIE) for 10 out of 11 emission scenarios, indicating global mass conservation in our simulation cases. Therefore, it is recommended that tracer emissions be assigned to model grid points with regular grid spacing for several adjacent model cells along the x, y, z directions.

We further investigated local mass conservation by mass-balance calculations over a sub-domain (control volume). Mass-balance calculations were conducted by considering a control volume (box) enclosing all emission sources. We estimated within-box source emission rates by calculating the net exiting flux through box top and lateral walls, and the temporal rate of change in tracer mass within the control volume. Under normal advective conditions (> 5 m/s wind speeds), the horizontal advective flux was equal to over 90% of the emission rate while turbulent fluxes were less than 2%. The remaining contribution came from the storage rate term, the release/accumulation rate of tracer mass within the control volume. Our mass-balance estimates were within 5% of MIE for tracer sources with release heights within the bottom 40 model vertical layers (with regular vertical grid spacing) for our three case studies (30 emission scenarios), indicating local mass conservation for our super-resolution WRF simulations. Again, this suggests that assigning tracer release on a regular grid (horizontal and vertical) would ensure mass conservation using the available WRF model mass conservation schemes.

Except for one hypothetical emission source, our results for various tracer emission scenarios under different meteorological conditions were globally and locally mass conserved within 4% and 5% of model input emission rates, respectively. In Fathi (2022) we use the model output from super-resolution WRF simulations discussed here for a model-based study of airborne top-down source emission rate retrievals. We evaluate the conventional methods and propose improved approaches for aircraft-based retrievals.

Code and data availability. The release version of WRF-ARW 3.9 used for this study can be downloaded from https://www2.mmm.ucar.edu /wrf/users/download/get_source.html. The North American Regional Reanalysis (NARR) data from National Oceanic and Atmospheric
595 Administration (NOAA) used as initial and boundary condition for model simulations in this study can be accessed at NOAA-Fathi (2022). The historical observational monitoring data from Wood Buffalo Environmental Association (WBEA) used for comparison to model output in this work can be accessed at WBEA-Fathi (2022). The aircraft measurements data from JOSM 2013 campagin used in this work are avaibale from Environment and Climate Change Canada Data Catalogue (ECCC, 2013).

Appendix A: Prognostic TKE Closure

600 The WRF model eddy viscosity (diffusivity) for the predicted turbulent kinetic energy option (K option *km_opt*= 2), are computed using (Skamarock et al., 2008),

$$K_{h,v} = C_k l_{h,v} \sqrt{e} \qquad (A1)$$

where e is the turbulent kinetic energy (prognostic in this scheme), C_k is a constant (typically $0.15 < C_k < 0.25$), and l is a length scale given as follows for the anisotropic option,

605 $$l_h = \sqrt{\Delta x \Delta y} \qquad (A2)$$

and,

$$l_v = \quad \min \left[\Delta z, 0.76 \sqrt{e}/N \right] \quad \text{for } N^2 > 0 \qquad (A3)$$

$$l_v = \qquad \Delta z \qquad\qquad \text{for } N^2 \leq 0. \qquad (A4)$$

where N is Brunt-Väisälä frequency, see Skamarock et al. (2008) for derivations. The eddy viscosity used for mixing scalars
610 is divided by a turbulent Prandtl number P_r. The Prandtl number is $1/3$ for the horizontal eddy viscosity K_h, and $P_r^{-1} = 1 + 2l/\Delta z$ for the vertical eddy viscosity K_v. Note that the above are for the anisotropic mixing option (mix_isotropic = 0, default) that was used in our WRF simulations.

Appendix B: Mass-balance turbulent flux terms

Derivations for turbulent flux terms in mass-balance equation Eq. 1,

615 $$F_{C,HT}(t) = - \iint K_h \frac{d\chi_C}{dx_\perp}(t,s,z)dsdz \qquad (B1)$$

$$F_{C,VT}(t) = - \iint K_v \frac{d\chi_C}{dz_\perp}(t,x,y)dxdy \qquad (B2)$$

where K_h and K_v are horizontal and vertical eddy diffusivity coefficients, respectively (see A). $d\chi_C/dx_\perp$ and $d\chi_C/dz_\perp$ are tracer concentration gradients across box lateral and top walls.

Appendix C: WRF model output meteorology profiles for the three case studies
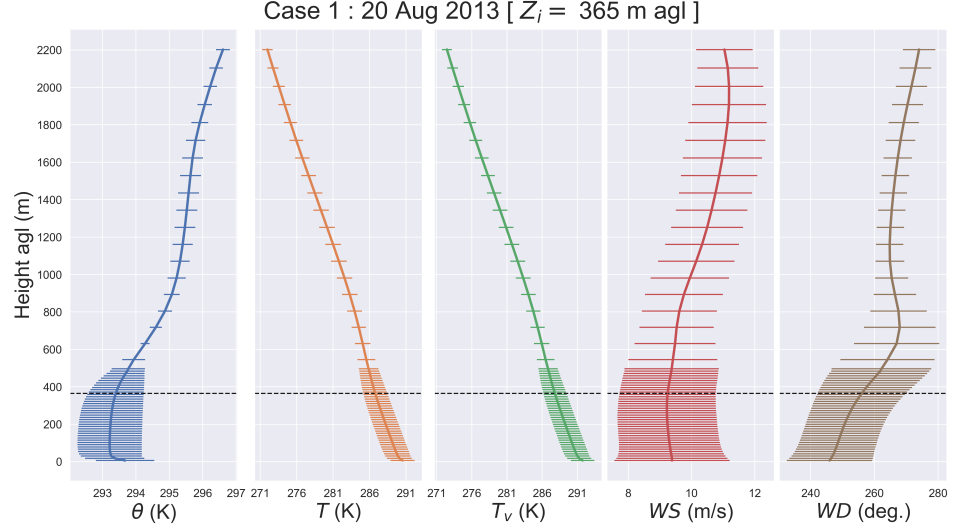
Figure C1. Case 1 meteorological profiles on 20 August 2013: potential temperature θ, absolute temperature T, virtual temperature T_v, wind speed WS, and wind direction WD. The profiles were averaged horizontally over domain d05 and over the simulation time. Bars show standard deviations. Inversion height Z_i is marked with dashed line.
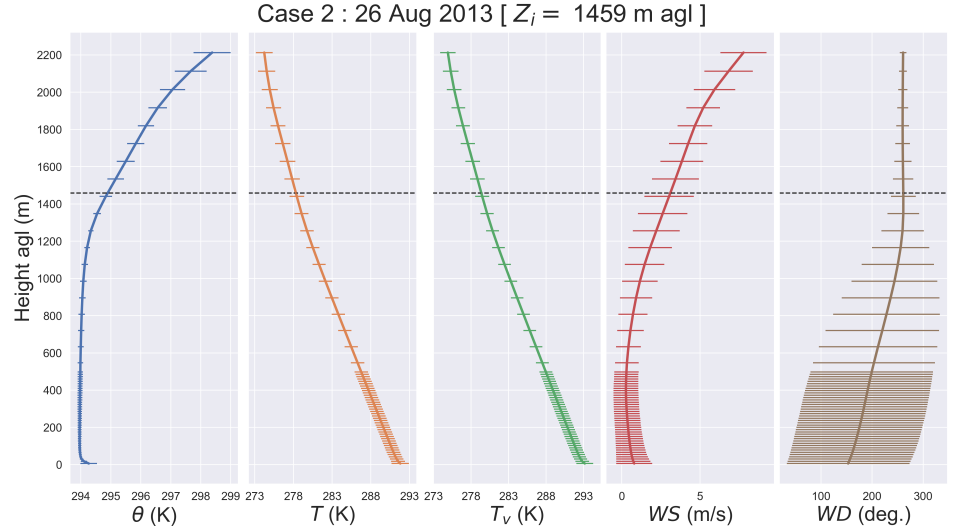
Figure C2. Case 2 meteorological profiles on 26 August 2013: potential temperature θ, absolute temperature T, virtual temperature T_v, wind speed WS, and wind direction WD. The profiles were averaged horizontally over domain d05 and over the simulation time. Bars show standard deviations. Inversion height Z_i is marked with dashed line.
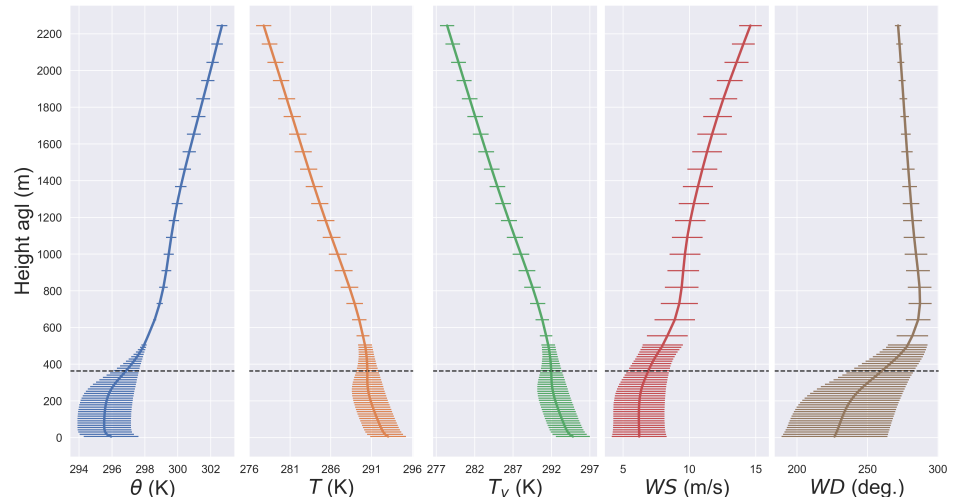
Figure C3. Case 3 meteorological profiles on 2 September 2013: potential temperature θ, absolute temperature T, virtual temperature T_v, wind speed WS, and wind direction WD. The profiles were averaged horizontally over domain d05 and over the simulation time. Bars show standard deviations. Inversion height Z_i is marked with dashed line.

Author contributions. SF setup and ran the WRF-ARW simulations, performed all the analysis using the model output data, and wrote the paper. MG and YC provided advice during planning and analysis and contributed to paper revisions.

Competing interests. The authors declare that they have no conflict of interest.

Acknowledgements. This research was enabled in part by support provided by Compute Ontario (Graham, graham.computecanada.ca), WestGrid (Cedar, cedar.computecanada.ca) and the Digital Research Alliance of Canada (alliancecan.ca). We acknowledge use of flight parameter information from the ECCC Data Catalogue: Pollutant Transformation, Summer 2013 Aircraft Intensive Multi Parameters, Oil Sands Region.

References

American Meteorological Society, 2021: Gradient Richardson number. Glossary of Meteorology, http://glossary.ametsoc.org/wiki/Gradient_richardson_number, 2022.

630 Ahmadov, R., McKeen, S., Trainer, M., Banta, R., Brewer, A., Brown, S., Edwards, P. M., de Gouw, J. A., Frost, G. J., Gilman, J., Helmig, D., Johnson, B., Karion, A., Koss, A., Langford, A., Lerner, B., Olson, J., Oltmans, S., Peischl, J., Pétron, G., Pichugina, Y., Roberts, J. M., Ryerson, T., Schnell, R., Senff, C., Sweeney, C., Thompson, C., Veres, P. R., Warneke, C., Wild, R., Williams, E. J., Yuan, B., and Zamora, R.: Understanding high wintertime ozone pollution events in an oil- and natural gas-producing region of the western US, Atmospheric Chemistry and Physics, 15, 411–429, https://doi.org/10.5194/acp-15-411-2015, 2015.

635 Alfieri, S., Amato, U., Carfora, M., Esposito, M., and Magliulo, V.: Quantifying trace gas emissions from composite landscapes: A mass-budget approach with aircraft measurements, Atmospheric Environment, 44, 1866–1876, https://doi.org/https://doi.org/10.1016/j.atmosenv.2010.02.026, 2010.

Angevine, W. M., Peischl, J., Crawford, A., Loughner, C. P., Pollack, I. B., and Thompson, C. R.: Errors in top-down estimates of emissions using a known source, Atmospheric Chemistry and Physics, 20, 11 855–11 868, https://doi.org/10.5194/acp-20-11855-2020, 2020.

640 Barkley, Z. R., Lauvaux, T., Davis, K. J., Deng, A., Miles, N. L., Richardson, S. J., Cao, Y., Sweeney, C., Karion, A., Smith, M., Kort, E. A., Schwietzke, S., Murphy, T., Cervone, G., Martins, D., and Maasakkers, J. D.: Quantifying methane emissions from natural gas production in north-eastern Pennsylvania, Atmospheric Chemistry and Physics, 17, 13 941–13 966, https://doi.org/10.5194/acp-17-13941-2017, 2017.

Blaylock, B. K.: Tracer Plumes in WRF (last accessed: March 8, 2023), https://home.chpc.utah.edu/~u0553130/Brian_Blaylock/tracer.html, 2017.

645 Blaylock, B. K., Horel, J. D., and Crosman, E. T.: Impact of Lake Breezes on Summer Ozone Concentrations in the Salt Lake Valley, Journal of Applied Meteorology and Climatology, 56, 353–370, https://doi.org/10.1175/JAMC-D-16-0216.1, 2017.

Conley, S., Faloona, I., Mehrotra, S., Suard, M., Lenschow, D. H., Sweeney, C., Herndon, S., Schwietzke, S., Pétron, G., Pifer, J., Kort, E. A., and Schnell, R.: Application of Gauss's theorem to quantify localized surface emissions from airborne measurements of wind and trace gases, Atmospheric Measurement Techniques, 10, 3345–3358, https://doi.org/10.5194/amt-10-3345-2017, 2017.

650 Cui, Y. Y., Brioude, J., McKeen, S. A., Angevine, W. M., Kim, S.-W., Frost, G. J., Ahmadov, R., Peischl, J., Bousserez, N., Liu, Z., Ryerson, T. B., Wofsy, S. C., Santoni, G. W., Kort, E. A., Fischer, M. L., and Trainer, M.: Top-down estimate of methane emissions in California using a mesoscale inverse modeling technique: The South Coast Air Basin, Journal of Geophysical Research: Atmospheres, 120, 6698–6711, https://doi.org/https://doi.org/10.1002/2014JD023002, 2015.

Daniels, M. H., Lundquist, K. A., Mirocha, J. D., Wiersema, D. J., and Chow, F. K.: A New Vertical Grid Nesting Capability in the Weather 655 Research and Forecasting (WRF) Model, Monthly Weather Review, 144, 3725–3747, https://doi.org/10.1175/MWR-D-16-0049.1, 2016.

ECCC: Pollutant Transformation, Summer 2013 Aircraft Intensive Multi Parameters, Oil Sands Region, https://data-donnees.ec.gc.ca/data/air/monitor/ambient-air-quality-oil-sands-region/pollutant-transformation-aircraft-based-multi-parameters-oil-sands-region/?lang=en, 2013.

Fathi, S.: Evaluating the Top-down Emission Rate Retrieval Algorithm (TERRA) Using Virtual Aircraft-based Sampling Within the GEM- 660 MACH Model, Master's thesis, York University, http://hdl.handle.net/10315/34547, 2017.

Fathi, S.: Optimizing Top-down Airborne Emission Retrievals through High and Super-Resolution Numerical Modelling, Dissertation, http://hdl.handle.net/10315/40663, 2022.

Fathi, S., Gordon, M., Makar, P. A., Akingunola, A., Darlington, A., Liggio, J., Hayden, K., and Li, S.-M.: Evaluating the impact of storage-and-release on aircraft-based mass-balance methodology using a regional air-quality model, Atmospheric Chemistry and Physics, 21, 15 461–15 491, https://doi.org/10.5194/acp-21-15461-2021, 2021.

665   Gasch, P., Wieser, A., Lundquist, J. K., and Kalthoff, N.: An LES-based airborne Doppler lidar simulator and its application to wind profiling in inhomogeneous flow conditions, Atmospheric Measurement Techniques, 13, 1609–1631, https://doi.org/10.5194/amt-13-1609-2020, 2020.

Gordon, M., Li, S.-M., Staebler, R., Darlington, A., Hayden, K., O'Brien, J., and Wolde, M.: Determining air pollutant emission rates based on mass balance using airborne measurement data over the Alberta oil sands operations, Atmospheric Measurement Techniques, 8, 3745–3765, https://doi.org/10.5194/amt-8-3745-2015, 2015.

Gordon, M., Makar, P. A., Staebler, R. M., Zhang, J., Akingunola, A., Gong, W., and Li, S.-M.: A comparison of plume rise algorithms to stack plume measurements in the Athabasca oil sands, Atmospheric Chemistry and Physics, 18, 14 695–14 714, https://doi.org/10.5194/acp-18-14695-2018, 2018.

675   Jacobson, M. Z.: Fundamentals of Atmospheric Modeling, Cambridge University Press, 2 edn., 2005.

JOSM: Joint Oil Sands Monitoring Plan, Integrated Monitoring Plan for the Oil Sands, Air Quality Component, p. 72, 2013.

Karion, A., Sweeney, C., Kort, E. A., Shepson, P. B., Brewer, A., Cambaliza, M., Conley, S. A., Davis, K., Deng, A., Hardesty, M., Herndon, S. C., Lauvaux, T., Lavoie, T., Lyon, D., Newberger, T., Pétron, G., Rella, C., Smith, M., Wolter, S., Yacovitch, T. I., and Tans, P.: Aircraft-Based Estimate of Total Methane Emissions from the Barnett Shale Region, Environmental Science & Technology, 49, 8124–8131, https://doi.org/10.1021/acs.est.5b00217, pMID: 26148550, 2015.

Kia, S., Flesch, T. K., Freeman, B. S., and Aliabadi, A. A.: Calculating gas emissions from open-pit mines using inverse dispersion modelling: A numerical evaluation using CALPUFF and CFD-LS, Journal of Wind Engineering and Industrial Aerodynamics, 226, 105 046, https://doi.org/https://doi.org/10.1016/j.jweia.2022.105046, 2022.

Knievel, J. C., Bryan, G. H., and Hacker, J. P.: Explicit Numerical Diffusion in the WRF Model, Monthly Weather Review, 135, 3808 – 3824, https://doi.org/10.1175/2007MWR2100.1, 2007.

Lauvaux, T., Miles, N. L., Deng, A., Richardson, S. J., Cambaliza, M. O., Davis, K. J., Gaudet, B., Gurney, K. R., Huang, J., O'Keefe, D., Song, Y., Karion, A., Oda, T., Patarasuk, R., Razlivanov, I., Sarmiento, D., Shepson, P., Sweeney, C., Turnbull, J., and Wu, K.: High-resolution atmospheric inversion of urban CO2 emissions during the dormant season of the Indianapolis Flux Experiment (INFLUX), Journal of Geophysical Research: Atmospheres, 121, 5213–5236, https://doi.org/https://doi.org/10.1002/2015JD024473, 2016.

690   Lee, D. and Tsuei, Y.: A formula for estimation of truncation errors of convection terms in a curvilinear coordinate system, Journal of Computational Physics, 98, 90 – 100, https://doi.org/https://doi.org/10.1016/0021-9991(92)90175-X, 1992.

Liu, Y., Warner, T., Liu, Y., Vincent, C., Wu, W., Mahoney, B., Swerdlin, S., Parks, K., and Boehnert, J.: Simultaneous nested modeling from the synoptic scale to the LES scale for wind energy applications, Journal of Wind Engineering and Industrial Aerodynamics, 99, 308–319, https://doi.org/https://doi.org/10.1016/j.jweia.2011.01.013, the Fifth International Symposium on Computational Wind Engineering, 2011.

Mohan, M. and Sati, A. P.: WRF model performance analysis for a suite of simulation design, Atmospheric Research, 169, 280–291, https://doi.org/https://doi.org/10.1016/j.atmosres.2015.10.013, 2016.

Nahian, M. R., Nazem, A., Nambiar, M. K., Byerlay, R., Mahmud, S., Seguin, A. M., Robe, F. R., Ravenhill, J., and Aliabadi, A. A.: Complex Meteorology over a Complex Mining Facility: Assessment of Topography, Land Use, and Grid Spacing Modifications in WRF, Journal of Applied Meteorology and Climatology, 59, 769 – 789, https://doi.org/10.1175/JAMC-D-19-0213.1, 2020.

NOAA-Fathi: North American Regional Reanalysis (NARR) data used in "Passive Tracer Modelling at Super- Resolution with WRF-ARW to Assess Mass-Balance Schemes", https://doi.org/10.5281/zenodo.7302357, 2022.

Onishi, R., Sugiyama, D., and Matsuda, K.: Super-Resolution Simulation for Real-Time Prediction of Urban Micrometeorology, SOLA, 15, 178–182, https://doi.org/10.2151/sola.2019-032, 2019.

705 Panitz, H.-J., Nester, K., and Fiedler, F.: Mass budget simulation of NOx and CO for the evaluation of calculated emissions for the city of Augsburg (Germany), Atmospheric Environment, 36, Supplement 1, 33 – 51, https://doi.org/http://dx.doi.org/10.1016/S1352-2310(02)00216-9, evaluation of Modeled Emission Inventories of Ozone Precursors. A Case Study for an Urban Area (Augsburg, Germany), 2002.

Peischl, J., Ryerson, T. B., Holloway, J. S., Parrish, D. D., Trainer, M., Frost, G. J., Aikin, K. C., Brown, S. S., Dubé, W. P., Stark, H.,
710 and Fehsenfeld, F. C.: A top-down analysis of emissions from selected Texas power plants during TexAQS 2000 and 2006, Journal of Geophysical Research: Atmospheres, 115, https://doi.org/https://doi.org/10.1029/2009JD013527, 2010.

Ražnjević, A., van Heerwaarden, C., van Stratum, B., Hensen, A., Velzeboer, I., van den Bulk, P., and Krol, M.: Technical note: Interpretation of field observations of point-source methane plume using observation-driven large-eddy simulations, Atmospheric Chemistry and Physics, 22, 6489–6505, https://doi.org/10.5194/acp-22-6489-2022, 2022.

715 Ryoo, J.-M., Iraci, L. T., Tanaka, T., Marrero, J. E., Yates, E. L., Fung, I., Michalak, A. M., Tadić, J., Gore, W., Bui, T. P., Dean-Day, J. M., and Chang, C. S.: Quantification of CO_2 and CH_4 emissions over Sacramento, California, based on divergence theorem using aircraft measurements, Atmospheric Measurement Techniques, 12, 2949–2966, https://doi.org/10.5194/amt-12-2949-2019, 2019.

Skamarock, W. C. and Weisman, M. L.: The Impact of Positive-Definite Moisture Transport on NWP Precipitation Forecasts, Monthly Weather Review, 137, 488–494, https://doi.org/10.1175/2008MWR2583.1, 2009.

720 Skamarock, W. C., Klemp, J. B., Dudhia, J., Gill, D. O., Barker, D., Duda, M. G., and Powers, J. G.: A Description of the Advanced Research WRF Version 3 (No. NCAR/TN-475+STR), University Corporation for Atmospheric Research, https://doi.org/doi:10.5065/D68S4MVH, 2008.

Watson, C. D., Wang, C., Lynar, T., and Weldemariam, K.: Investigating two super-resolution methods for downscaling precipitation: ESRGAN and CAR, https://doi.org/10.48550/ARXIV.2012.01233, 2020.

725 WBEA-Fathi: Wood Buffalo Environmental Association (WBEA) Historical Monitoring Data used in "Passive Tracer Modelling at Super-Resolution with WRF-ARW to Assess Mass-Balance Schemes", https://doi.org/10.5281/zenodo.7306284, 2022.

Wicker, L. J. and Skamarock, W. C.: Time-Splitting Methods for Elastic Models Using Forward Time Schemes, Monthly Weather Review, 130, 2088 – 2097, https://doi.org/10.1175/1520-0493(2002)130<2088:TSMFEM>2.0.CO;2, 2002.

Wu, Y., Teufel, B., Sushama, L., Belair, S., and Sun, L.: Deep Learning-Based Super-Resolution Climate Simulator-Emulator Framework for Urban Heat Studies, Geophysical Research Letters, 48, e2021GL094 737, https://doi.org/https://doi.org/10.1029/2021GL094737,
730 e2021GL094737 2021GL094737, 2021.

Xue, M.: High-Order Monotonic Numerical Diffusion and Smoothing, Monthly Weather Review, 128, 2853 – 2864, https://doi.org/10.1175/1520-0493(2000)128<2853:HOMNDA>2.0.CO;2, 2000.

You, D., Mittal, R., Wang, M., and Moin, P.: Analysis of stability and accuracy of finite-difference schemes on a skewed mesh, Journal of
735 Computational Physics, 213, 184 – 204, https://doi.org/https://doi.org/10.1016/j.jcp.2005.08.007, 2006.